

A Dissipation Theory for Three-Dimensional FDTD with Application to Stability Analysis and Subgridding

Fadime Bekmambetova, *Student Member, IEEE*, Xinyue Zhang *Student Member, IEEE*, and Piero Triverio, *Senior Member, IEEE*

Abstract—The finite-difference time-domain algorithm is a popular numerical method for solving electromagnetic problems. FDTD simulations can suffer from instability due to the explicit nature of the method. Enforcement of stability can be particularly challenging in scenarios where a setup is composed of multiple components, such as differently refined FDTD grids, macromodels, advanced boundary conditions, and others. Moreover, the lack of modularity in existing stability analysis methods can make small modifications to the system burdensome.

We propose a 3-D dissipativity framework that can be used to enforce stability of novel FDTD schemes in a modular fashion, which is an extension of previous developments in 2-D [1]. With this framework one can analyze parts of the system separately, which simplifies stability proofs and avoids the need to revise the entire proof when a single part of a system is changed. With these results, we derive a 3-D subgridding scheme with guaranteed stability, good accuracy, and support for any odd grid refinement ratios. Subgridding boundary is allowed to traverse different materials, producing meaningful results with no instability.

Index Terms—dissipativity, finite-difference time-domain, stability, subgridding

I. INTRODUCTION

Stability is a major challenge in explicit numerical schemes for solving differential equations. The stability analysis can be performed using different techniques such as Von Neumann analysis [2], iteration method [3] and energy method [4]. However, Von Neumann analysis is not applicable in many practical problems. Iteration and energy methods are more general, but they may lead to lengthy derivations when applied to systems consisting of many parts.

Maxwell's equations are often solved using the finite-difference time-domain (FDTD) method [5], which is stable when the iteration time step is below the Courant-Friedrichs-Lewy (CFL) limit [3]. However, the stability enforcement is more difficult for advanced FDTD-based schemes, which can involve many subsystems, such as locally refined grids [6–8], reduced order models [9], [10], hybridizations with other numerical methods [11–13], coupling of FDTD-derived models with circuit simulators [14], and other modifications to FDTD,

This work was supported in part by the Natural Sciences and Engineering Research Council of Canada (Discovery grant program) and in part by the Canada Research Chairs program.

F. Bekmambetova, X. Zhang and P. Triverio are with the Edward S. Rogers Sr. Department of Electrical and Computer Engineering, University of Toronto, Toronto, M5S 3G4 Canada (email: fadime.bekmambetova@mail.utoronto.ca, xinyue.zhang.zhang@mail.utoronto.ca, piero.triverio@utoronto.ca).

which are aimed at improving efficiency of the conventional algorithm.

In order to ensure that the numerical solutions do not diverge in time, one can apply the iteration method [3], [15] that analyzes the eigenvalues of a matrix describing FDTD iterations. This approach makes it nontrivial to take advantage of the stability properties of the conventional FDTD once it has been integrated with other subsystems. This limitation can make proofs conceptually difficult. Similar issue arises in the case of the energy method [4], where stability is proven by analyzing the energy of the entire setup, which may consist of many coupled subsystems. Stability analysis methods based on analyzing the associated hyperbolic equation have been proposed in literature [16], [17]. However those methods also do not offer a general strategy for complete conceptual decoupling of stability analysis for different subsystems.

In this paper, we present a dissipativity theory for modular stability enforcement of complex 3D FDTD systems, generalizing the previous work in two dimensions [1]. The proposed approach involves showing that all parts of the setup are unable to produce energy on their own. The method extends [4] by analyzing the power flow between subsystems, which allows the dissipativity conditions to be applied separately on individual components. This makes stability analysis simpler and more intuitive. Moreover, system that is analyzed with the proposed approach can be modified easily, without requiring revision of the entire stability proof. The 2-D dissipativity theory has been successfully applied to embedding macromodels in FDTD in a stable manner [18]. Here, we use the theory in three dimensions to derive a stable subgridding scheme that allows the use of any odd grid refinement ratio and naturally supports traversal of material boundaries by the subgridding interface.

This paper is structured as follows. In Sec. II we show how FDTD region can be cast into the form of a dynamical system with suitable inputs and outputs. In Sec. III we provide dissipativity conditions for the region and show their relation to the CFL limit. In Sec. IV we describe the modular method for enforcing FDTD stability using this result and in Sec. V we apply this method to derive a stable subgridding scheme. Numerical examples are provided Sec. VI.

II. DYNAMICAL SYSTEM FORMULATION OF A 3-D FDTD REGION

Consider the FDTD region shown in Fig. 1, which contains N_x , N_y , and N_z primary cells in x , y , and z directions,

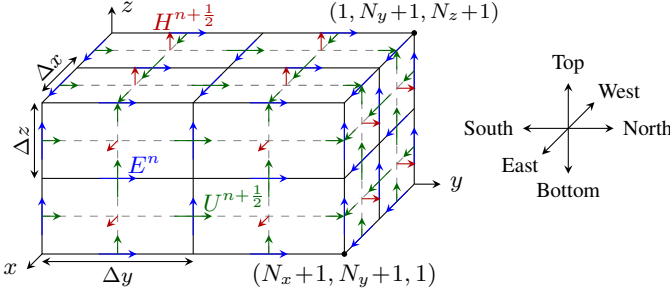


Fig. 1: Illustration of the 3-D FDTD region with the hanging variables shown in green. The secondary grid is shown with the dashed line.

respectively. Electric field is sampled at the primary grid edges (secondary grid faces) at the integer time points, n , and magnetic field is sampled at the secondary grid edges (primary grid faces) at the time points shifted by half of a time step, $n \pm (1/2)$ [3]. For simplicity, we assume that the region is discretized uniformly with primary cells of dimensions $\Delta x \times \Delta y \times \Delta z$.

In addition to the conventional electric and magnetic field samples, denoted by E^n and $H^{n \pm 1/2}$, respectively, we define the so-called hanging variables [19], $U^{n \pm (1/2)}$, which are magnetic field samples collocated with the electric fields directly at the boundary of the region. These hanging variables are used to define the power supplied to the region and to facilitate formulation of an FDTD grid as a self-contained system.

In this section, we take the equations describing the dynamics of electric and magnetic field samples, E^n and $H^{n-(1/2)}$, respectively, and cast them in the form of a dynamical system with the hanging variables, $U^{n+(1/2)}$, as its inputs. The output is formed using electric field samples directly on the boundary of the region.

A. Equations at Each Node

Dynamics of any electric field sample strictly inside the region, such as the $E_x|_{i+\frac{1}{2},j,k}^n$ sample shown in Fig. 2a, are described using the conventional FDTD update equation [3]

$$\begin{aligned} \Delta x \Delta y \Delta z \left(\frac{\varepsilon_x}{\Delta t} + \frac{\sigma_x}{2} \right) E_x|_{i+\frac{1}{2},j,k}^{n+1} \\ = \Delta x \Delta y \Delta z \left(\frac{\varepsilon_x}{\Delta t} - \frac{\sigma_x}{2} \right) E_x|_{i+\frac{1}{2},j,k}^n \\ - \Delta x \Delta y H_y|_{i+\frac{1}{2},j,k+\frac{1}{2}}^{n+\frac{1}{2}} + \Delta x \Delta y H_y|_{i+\frac{1}{2},j,k-\frac{1}{2}}^{n+\frac{1}{2}} \\ + \Delta x \Delta z H_z|_{i+\frac{1}{2},j+\frac{1}{2},k}^{n+\frac{1}{2}} - \Delta x \Delta z H_z|_{i+\frac{1}{2},j-\frac{1}{2},k}^{n+\frac{1}{2}}, \quad (1) \end{aligned}$$

where σ_x and ε_x are electrical conductivity and permittivity values, respectively, at the edge where the electric field is sampled. For clarity, we do not show dependence of material properties on the location. The iteration time step is denoted by Δt . Although Δx , the length of the edge at which the field is sampled, can be canceled, we keep it for later derivations.

The electric field samples on the region's faces, such as the South $E_x|_{i+(1/2),1,k}^n$ sample in Fig. 2b, do not have all

four $H^{n+1/2}$ samples that are necessary for completing the conventional FDTD equation. Indeed, the use of magnetic fields outside the region would require assumptions on the nature of subsystems connected to the FDTD grid. Instead, we write the modified equations for the South electric field samples using the hanging variables

$$\begin{aligned} \Delta x \frac{\Delta y}{2} \Delta z \left(\frac{\varepsilon_x}{\Delta t} + \frac{\sigma_x}{2} \right) E_x|_{i+\frac{1}{2},1,k}^{n+1} \\ = \Delta x \frac{\Delta y}{2} \Delta z \left(\frac{\varepsilon_x}{\Delta t} - \frac{\sigma_x}{2} \right) E_x|_{i+\frac{1}{2},1,k}^n \\ - \Delta x \frac{\Delta y}{2} H_y|_{i+\frac{1}{2},1,k+\frac{1}{2}}^{n+\frac{1}{2}} + \Delta x \frac{\Delta y}{2} H_y|_{i+\frac{1}{2},1,k-\frac{1}{2}}^{n+\frac{1}{2}} \\ + \Delta x \Delta z H_z|_{i+\frac{1}{2},\frac{3}{2},k}^{n+\frac{1}{2}} - \Delta x \Delta z U_z|_{i+\frac{1}{2},1,k}^{n+\frac{1}{2}}. \quad (2) \end{aligned}$$

This expression is obtained from the FDTD-like approximation of Maxwell-Ampère equation on a half-cell containing the boundary electric field sample. Equation (2) can be viewed as a general boundary condition for the FDTD region, which we use for connecting it to other subsystems.

The equations for the samples located at the edges where two faces of the boundary come together involve two hanging variables. For instance, in the case of the Bottom-South sample shown in Fig. 2c, the y - and z -directed hanging variables, $U_y|_{i+(1/2),1,1}^{n+\frac{1}{2}}$ and $U_z|_{i+(1/2),1,1}^{n+\frac{1}{2}}$, respectively, are used to complete the line integral of magnetic field around $E_x|_{i+(1/2),1,1}^n$

$$\begin{aligned} \Delta x \frac{\Delta y}{2} \frac{\Delta z}{2} \left(\frac{\varepsilon_x}{\Delta t} + \frac{\sigma_x}{2} \right) E_x|_{i+\frac{1}{2},1,1}^{n+1} \\ = \Delta x \frac{\Delta y}{2} \frac{\Delta z}{2} \left(\frac{\varepsilon_x}{\Delta t} - \frac{\sigma_x}{2} \right) E_x|_{i+\frac{1}{2},1,1}^n \\ - \Delta x \frac{\Delta y}{2} H_y|_{i+\frac{1}{2},1,\frac{3}{2}}^{n+\frac{1}{2}} + \Delta x \frac{\Delta y}{2} U_y|_{i+\frac{1}{2},1,1}^{n+\frac{1}{2}} \\ + \Delta x \frac{\Delta z}{2} H_z|_{i+\frac{1}{2},\frac{3}{2},1}^{n+\frac{1}{2}} - \Delta x \frac{\Delta z}{2} U_z|_{i+\frac{1}{2},1,1}^{n+\frac{1}{2}}. \quad (3) \end{aligned}$$

Dynamics of E_y^n and E_z^n are described similarly to those of the E_x^n component.

In the following discussion variables such as $E_x|_{i+(1/2),1,1}^n$, which are shared between two faces of the boundary will be referred to as Type II quantities, whereas the variables belonging to a single face of the boundary will be classified as Type I.

For the conventional magnetic field samples, we take the standard FDTD equations, multiplied by the length of the secondary edge at which the field is sampled. This way, the equations for the internal magnetic $H_x^{n-(1/2)}$ samples read

$$\begin{aligned} \Delta x \Delta y \Delta z \frac{\mu_x}{\Delta t} H_x|_{i,j+\frac{1}{2},k+\frac{1}{2}}^{n+\frac{1}{2}} = \Delta x \Delta y \Delta z \frac{\mu_x}{\Delta t} H_x|_{i,j+\frac{1}{2},k+\frac{1}{2}}^{n-\frac{1}{2}} \\ + \Delta x \Delta y E_y|_{i,j+\frac{1}{2},k+1}^n - \Delta x \Delta y E_y|_{i,j+\frac{1}{2},k}^n \\ - \Delta x \Delta z E_z|_{i,j+1,k+\frac{1}{2}}^n + \Delta x \Delta z E_z|_{i,j,k+\frac{1}{2}}^n, \quad (4) \end{aligned}$$

where μ_x is the magnetic permeability at the sampling location. Equations for the samples at the West boundary involve

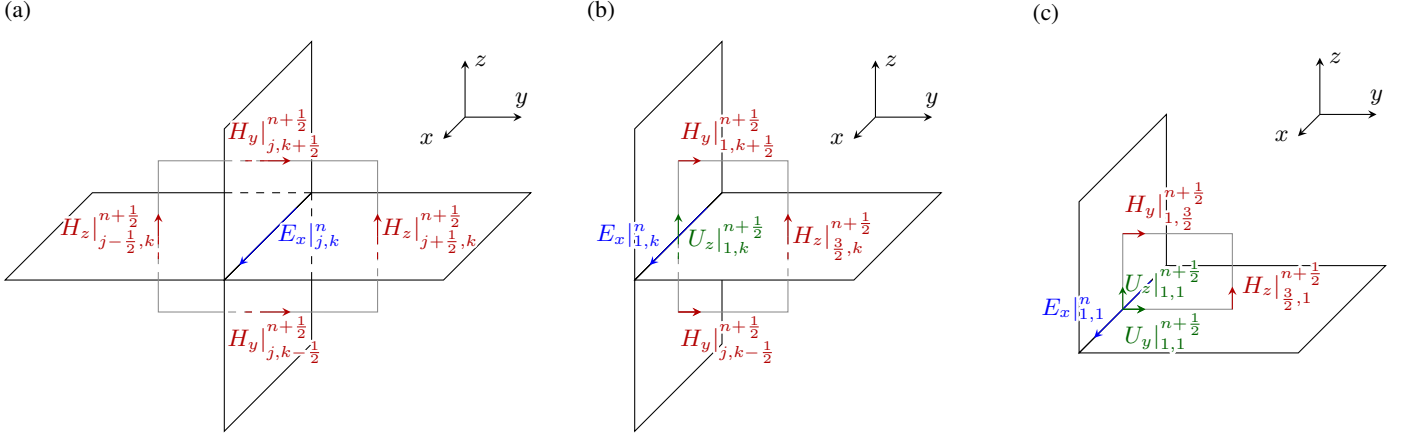


Fig. 2: Variables involved in the equations for (a) internal E_x samples, (b) E_x samples of Type I on the South face, and (c) the E_x samples of Type II at the Bottom-South edge of the boundary. The common subscript “ $i + (1/2)$ ” is omitted for clarity.

a factor of $\Delta x/2$, as opposed to Δx

$$\begin{aligned} \frac{\Delta x}{2} \Delta y \Delta z \frac{\mu_x}{\Delta t} H_x |_{1,j+\frac{1}{2},k+\frac{1}{2}}^{n+\frac{1}{2}} &= \frac{\Delta x}{2} \Delta y \Delta z \frac{\mu_x}{\Delta t} H_x |_{1,j+\frac{1}{2},k+\frac{1}{2}}^{n-\frac{1}{2}} \\ &+ \frac{\Delta x}{2} \Delta y E_y |_{1,j+\frac{1}{2},k+1}^n - \frac{\Delta x}{2} \Delta y E_y |_{1,j+\frac{1}{2},k}^n \\ &- \frac{\Delta x}{2} \Delta z E_z |_{1,j+1,k+\frac{1}{2}}^n + \frac{\Delta x}{2} \Delta z E_z |_{1,j,k+\frac{1}{2}}^n, \end{aligned} \quad (5)$$

and similarly for the boundary faces on the East. Equations for $H_y^{n-(1/2)}$ and $H_z^{n-(1/2)}$ are written in a similar fashion.

We write the equations in Sec. II-A in a matrix form. This way, equation for $H_x^{n-(1/2)}$ samples resulting from (4) and (5) reads as follows

$$\begin{aligned} \mathbf{D}_{l'_x} \mathbf{D}_{A_x} \frac{\mathbf{D}_{\mu_x}}{\Delta t} \mathbf{H}_x^{n+\frac{1}{2}} &= \mathbf{D}_{l'_x} \mathbf{D}_{A_x} \frac{\mathbf{D}_{\mu_x}}{\Delta t} \mathbf{H}_x^{n-\frac{1}{2}} \\ &+ \mathbf{D}_{l'_x} \mathbf{G}_{zE_y} \mathbf{D}_{l'_y} \mathbf{E}_y^n - \mathbf{D}_{l'_x} \mathbf{G}_{yE_z} \mathbf{D}_{l'_z} \mathbf{E}_z^n, \end{aligned} \quad (6)$$

where the vectors $\mathbf{H}_x^{n-(1/2)}$ and \mathbf{E}_y^n contain all $H_x^{n-(1/2)}$ and E_y^n samples of the region, respectively. The coefficient matrix \mathbf{D}_{μ_x} is a diagonal matrix containing magnetic permeability values at the x -directed secondary edges. Matrix \mathbf{G}_{zE_y} , which consists of zeros, +1's and -1's, is a discrete z -derivative operator for E_y . Similarly, \mathbf{G}_{yE_z} is a discrete y -derivative operator for E_z . Matrix $\mathbf{D}_{l'_x}$ is a diagonal matrix containing the x -directed secondary edge lengths, whose values are equal to Δx at the internal edges and to $\Delta x/2$ at the West and East faces of the region's boundary. The diagonal matrix \mathbf{D}_{A_x} contains the areas of primary faces with the x -directed normal vectors. With the uniform discretization, \mathbf{D}_{A_x} reduces to $\Delta y \Delta z \mathbf{I}_{N_{H_x}}$, where \mathbf{I}_m denotes an $m \times m$ identity matrix and N_{H_x} is the number of $H_x^{n-(1/2)}$ samples. It should be mentioned that the product $\mathbf{D}_{l'_x} \mathbf{D}_{A_x}$ is a diagonal matrix containing the volumes associated with each $H_x^{n-(1/2)}$ sample in $\mathbf{H}_x^{n-(1/2)}$. The diagonal matrices $\mathbf{D}_{l'_y}$ and $\mathbf{D}_{l'_z}$ contain x - and y -directed primary edge lengths, respectively. These reduce to $\Delta y \mathbf{I}_{N_{E_y}}$ and $\Delta z \mathbf{I}_{N_{E_z}}$ for uniform discretization. Equations for $\mathbf{H}_y^{n-(1/2)}$ and $\mathbf{H}_z^{n-(1/2)}$ have the form similar to (6).

From (1), (2), and (3), the matrix equation for the E_x^n samples can be written as follows

$$\begin{aligned} \mathbf{D}_{l_x} \mathbf{D}_{A'_x} \left(\frac{\mathbf{D}_{\varepsilon_x}}{\Delta t} + \frac{\mathbf{D}_{\sigma_x}}{2} \right) \mathbf{E}_x^{n+1} &= \mathbf{D}_{l_x} \mathbf{D}_{A'_x} \left(\frac{\mathbf{D}_{\varepsilon_x}}{\Delta t} - \frac{\mathbf{D}_{\sigma_x}}{2} \right) \mathbf{E}_x^n \\ &+ \mathbf{D}_{l_x} \mathbf{G}_{zE_x}^T \mathbf{D}_{l'_y} \mathbf{H}_y^{n+\frac{1}{2}} - \mathbf{D}_{l_x} \mathbf{G}_{yE_x}^T \mathbf{D}_{l'_z} \mathbf{H}_z^{n+\frac{1}{2}} \\ &+ \mathbf{D}_{l_x} \mathbf{B}_{E_x,B} \mathbf{D}_{l'_{y,B}} \mathbf{U}_{y,B}^{n+\frac{1}{2}} + \mathbf{D}_{l_x} \mathbf{B}_{E_x,N} \mathbf{D}_{l'_{z,N}} \mathbf{U}_{z,N}^{n+\frac{1}{2}} \\ &- \mathbf{D}_{l_x} \mathbf{B}_{E_x,T} \mathbf{D}_{l'_{y,T}} \mathbf{U}_{y,T}^{n+\frac{1}{2}} - \mathbf{D}_{l_x} \mathbf{B}_{E_x,S} \mathbf{D}_{l'_{z,S}} \mathbf{U}_{z,S}^{n+\frac{1}{2}}, \end{aligned} \quad (7)$$

where $\mathbf{D}_{\varepsilon_x}$ and \mathbf{D}_{σ_x} are diagonal matrices with the values of permittivity and electric conductivity, respectively, at the x -directed primary edges. The diagonal matrix $\mathbf{D}_{A'_x}$ contains the areas of secondary faces at which E_x^n is sampled, which equal to $\Delta y \Delta z$ for the internal nodes, $\Delta y \Delta z/2$ for Type I boundary nodes, and $\Delta y \Delta z/4$ for Type II nodes. Matrix $\mathbf{B}_{E_x,B}$ consists of 0's and 1's that map the Bottom y -directed hanging variables to the corresponding elements in \mathbf{E}_x^n . Matrices $\mathbf{B}_{E_x,T}$, $\mathbf{B}_{E_x,S}$, and $\mathbf{B}_{E_x,N}$ serve the analogous purpose. In a similar manner, we write the matrix equations for \mathbf{E}_y^n and \mathbf{E}_z^n , which, combined with (7) yield

$$\begin{aligned} \mathbf{D}_l \mathbf{D}_{A'} \left(\frac{\mathbf{D}_\varepsilon}{\Delta t} + \frac{\mathbf{D}_\sigma}{2} \right) \mathbf{E}^{n+1} &= \mathbf{D}_l \mathbf{D}_{A'} \left(\frac{\mathbf{D}_\varepsilon}{\Delta t} - \frac{\mathbf{D}_\sigma}{2} \right) \mathbf{E}^n \\ &+ \mathbf{D}_l \mathbf{C}^T \mathbf{D}_{l'} \mathbf{H}^{n+\frac{1}{2}} + \mathbf{D}_l \mathbf{B}_E \mathbf{D}_{l'_U} \mathbf{U}^{n+\frac{1}{2}}. \end{aligned} \quad (8a)$$

Equation describing the recurrence relation for all conventional magnetic field variables reads

$$\mathbf{D}_{l'} \mathbf{D}_A \frac{\mathbf{D}_\mu}{\Delta t} \mathbf{H}^{n+\frac{1}{2}} = \mathbf{D}_{l'} \mathbf{D}_A \frac{\mathbf{D}_\mu}{\Delta t} \mathbf{H}^{n-\frac{1}{2}} - \mathbf{D}_{l'} \mathbf{C} \mathbf{D}_l \mathbf{E}^n. \quad (8b)$$

In (8a)–(8b), vectors \mathbf{E}^n and \mathbf{H}^n collect all electric and conventional magnetic field variables, respectively

$$\mathbf{E}^n = \begin{bmatrix} \mathbf{E}_x^n \\ \mathbf{E}_y^n \\ \mathbf{E}_z^n \end{bmatrix}, \quad \mathbf{H}^{n-\frac{1}{2}} = \begin{bmatrix} \mathbf{H}_x^{n-\frac{1}{2}} \\ \mathbf{H}_y^{n-\frac{1}{2}} \\ \mathbf{H}_z^{n-\frac{1}{2}} \end{bmatrix}. \quad (9)$$

Matrices \mathbf{D}_l and $\mathbf{D}_{A'}$ contain in the diagonal entries all primary edge lengths and secondary face areas associated with the electric field samples. Diagonal matrices $\mathbf{D}_{l'}$ and

\mathbf{D}_A contain the edge lengths and face areas associated with magnetic field samples and matrices \mathbf{D}_ε , \mathbf{D}_μ , and \mathbf{D}_σ contain permittivity, permeability, and electrical conductivity. Coefficient matrix \mathbf{C} is a discrete curl operator

$$\mathbf{C} = \begin{bmatrix} 0 & -\mathbf{G}_{zE_y} & \mathbf{G}_{yE_z} \\ \mathbf{G}_{zE_x} & 0 & -\mathbf{G}_{xE_z} \\ -\mathbf{G}_{yE_x} & \mathbf{G}_{xE_y} & 0 \end{bmatrix}. \quad (10)$$

Matrix \mathbf{B}_E maps the hanging variables with appropriate signs to the electric fields with which they are associated

$$\mathbf{B}_E = \begin{bmatrix} \mathbf{B}_{E_x} & \mathbf{0} & \mathbf{0} \\ \mathbf{0} & \mathbf{B}_{E_y} & \mathbf{0} \\ \mathbf{0} & \mathbf{0} & \mathbf{B}_{E_z} \end{bmatrix}, \quad (11)$$

where

$$\mathbf{B}_{E_x} = [\mathbf{B}_{E_x,B} \quad -\mathbf{B}_{E_x,T} \quad -\mathbf{B}_{E_x,S} \quad \mathbf{B}_{E_x,N}], \quad (12a)$$

$$\mathbf{B}_{E_y} = [-\mathbf{B}_{E_y,B} \quad \mathbf{B}_{E_y,T} \quad \mathbf{B}_{E_y,W} \quad -\mathbf{B}_{E_y,E}], \quad (12b)$$

$$\mathbf{B}_{E_z} = [\mathbf{B}_{E_z,S} \quad -\mathbf{B}_{E_z,N} \quad -\mathbf{B}_{E_z,W} \quad \mathbf{B}_{E_z,E}]. \quad (12c)$$

Matrix \mathbf{D}'_U in (8a) is a diagonal matrix containing the lengths of the edges on which the hanging variables are sampled.

B. Dynamical System Formulation

The matrix equations (8a)–(8b) can be written in the form of a dynamical system as follows [1]

$$(\mathbf{R} + \mathbf{F})\mathbf{x}^{n+1} = (\mathbf{R} - \mathbf{F})\mathbf{x}^n + \mathbf{B}\mathbf{u}^{n+\frac{1}{2}}, \quad (13a)$$

$$\mathbf{y}^n = \mathbf{L}^T \mathbf{x}^n, \quad (13b)$$

where the state vector \mathbf{x}^n contains the conventional FDTD samples of the region

$$\mathbf{x}^n = \begin{bmatrix} \mathbf{E}^n \\ \mathbf{H}^{n-\frac{1}{2}} \end{bmatrix}, \quad (14)$$

and the input vector $\mathbf{u}^{n+\frac{1}{2}}$ is the vector of hanging variables

$$\mathbf{u}^{n+\frac{1}{2}} = \begin{bmatrix} \mathbf{U}^{n+\frac{1}{2}}_{E_x} \\ \mathbf{U}^{n+\frac{1}{2}}_{E_y} \\ \mathbf{U}^{n+\frac{1}{2}}_{E_z} \end{bmatrix}. \quad (15)$$

In the definition (15), vector $\mathbf{U}^{n+(1/2)}_{E_x}$ collects the variables associated with the E_x^n samples. Similar notation is used for the vectors $\mathbf{U}^{n+(1/2)}_{E_y}$ and $\mathbf{U}^{n+(1/2)}_{E_z}$. Matrices \mathbf{R} and \mathbf{F} and \mathbf{B} are shown below

$$\mathbf{R} = \begin{bmatrix} \mathbf{D}_l \mathbf{D}_{A'} \frac{\mathbf{D}_\varepsilon}{\Delta t} & -\frac{1}{2} \mathbf{D}_l \mathbf{C}^T \mathbf{D}_{l'} \\ -\frac{1}{2} \mathbf{D}_{l'} \mathbf{C} \mathbf{D}_l & \mathbf{D}_{l'} \mathbf{D}_A \frac{\mathbf{D}_\mu}{\Delta t} \end{bmatrix}, \quad (16a)$$

$$\mathbf{F} = \begin{bmatrix} \mathbf{D}_l \mathbf{D}_{A'} \frac{\mathbf{D}_\sigma}{2} & -\frac{1}{2} \mathbf{D}_l \mathbf{C}^T \mathbf{D}_{l'} \\ \frac{1}{2} \mathbf{D}_{l'} \mathbf{C} \mathbf{D}_l & \mathbf{0} \end{bmatrix}, \quad (16b)$$

$$\mathbf{B} = \begin{bmatrix} \mathbf{D}_l \mathbf{B}_E \mathbf{D}'_U \\ \mathbf{0} \end{bmatrix}. \quad (16c)$$

The matrix \mathbf{L}^T in (13b) maps the state vector, \mathbf{x}^n , to the output vector, \mathbf{y}^n .

The elements of \mathbf{y}^n have a one-to-one correspondence with those of $\mathbf{u}^{n+(1/2)}$ in terms of their quantity and ordering. In particular, the hanging variables in $\mathbf{u}^{n+(1/2)}$ sampled at Type I

nodes each have a corresponding electric field sample in \mathbf{y}^n at the same entry. Since two hanging variables are associated with each electric field sample of Type II, each such E^n appears twice in the vector \mathbf{y}^n with a factor of $1/\sqrt{2}$. The positions in the vector $\mathbf{u}^{n+(1/2)}$ or, equivalently, in \mathbf{y}^n will henceforth be referred to as ‘‘ports’’, since they define input-output pairs for the system (13a)–(13b).

To achieve the aforementioned structure of the vector \mathbf{y}^n , the matrix \mathbf{L}^T contains three types of columns

$$\mathbf{L}^T = \begin{bmatrix} \cdots & \mathbf{0} & \cdots & \mathbf{e}_{p_1} & \cdots & \tilde{\mathbf{e}}_{p_2,p_3} & \cdots \end{bmatrix}. \quad (17)$$

The zero columns correspond to internal electric field samples, which are not mapped to any output variables. Each column of the form \mathbf{e}_{p_1} maps a boundary electric field sample of Type I to its corresponding port p_1 . These columns contain a single 1 in the position p_1 . Columns of the form $\tilde{\mathbf{e}}_{p_2,p_3}$ correspond to the electric field samples of Type II. These columns contain two $1/\sqrt{2}$ entries in positions p_2 and p_3 in order to map the each electric field sample to the corresponding pair of ports

$$\tilde{\mathbf{e}}_{p_2,p_3} = \begin{bmatrix} \cdots & \frac{1}{\sqrt{2}} & \cdots & \frac{1}{\sqrt{2}} & \cdots \end{bmatrix}^T. \quad (18)$$

III. DISSIPATIVITY OF 3D FDTD REGION

As in [1], we define the storage function $\mathcal{E}(\mathbf{x}^n)$ for the FDTD region, which quantifies the energy stored in the system, and the supply rate, $s(\mathbf{y}^n, \mathbf{u}^{n+(1/2)})$ which is the energy absorbed by the region through its boundaries between time points n and $n+1$. The system (13a)–(13b) is dissipative with the supply rate $s(\mathbf{y}^n, \mathbf{u}^{n+\frac{1}{2}})$ if we can find a function that satisfies [20]

$$\mathcal{E}(\mathbf{x}^n) \geq 0, \quad \forall \mathbf{x}^n, \quad (19a)$$

$$\mathcal{E}(\mathbf{0}) = 0, \quad (19b)$$

$$\mathcal{E}(\mathbf{x}^{n+1}) - \mathcal{E}(\mathbf{x}^n) \leq s(\mathbf{y}^n, \mathbf{u}^{n+\frac{1}{2}}), \quad \forall \mathbf{u}^{n+\frac{1}{2}}, \quad \forall n. \quad (19c)$$

Following [1], we define the storage function and the supply rate as

$$\mathcal{E}(\mathbf{x}^n) = \frac{\Delta t}{2} (\mathbf{x}^n)^T \mathbf{R} \mathbf{x}^n, \quad (20a)$$

$$s(\mathbf{y}^n, \mathbf{u}^{n+\frac{1}{2}}) = \Delta t \frac{(\mathbf{y}^n + \mathbf{y}^{n+1})^T}{2} \mathbf{L}^T \mathbf{B} \mathbf{u}^{n+\frac{1}{2}}. \quad (20b)$$

A. Physical Meaning of the Supply Rate and Storage Function

By substituting (14) and (16a) into (20a), we can write the storage function as follows

$$\begin{aligned} \mathcal{E}(\mathbf{x}^n) &= \frac{1}{2} (\mathbf{E}^n)^T \mathbf{D}_l \mathbf{D}_{A'} \mathbf{D}_\varepsilon \mathbf{E}^n \\ &+ \frac{\Delta t}{2} (\mathbf{H}^{n-\frac{1}{2}})^T \left[\mathbf{D}_{l'} \mathbf{D}_A \frac{\mathbf{D}_\mu}{\Delta t} \mathbf{H}^{n-\frac{1}{2}} - \mathbf{D}_{l'} \mathbf{C} \mathbf{D}_l \mathbf{E}^n \right], \end{aligned} \quad (21)$$

which, using (8b), reduces to

$$\begin{aligned} \mathcal{E}(\mathbf{x}^n) &= \frac{1}{2} (\mathbf{E}^n)^T \mathbf{D}_l \mathbf{D}_{A'} \mathbf{D}_\varepsilon \mathbf{E}^n \\ &+ \frac{1}{2} (\mathbf{H}^{n-\frac{1}{2}})^T \mathbf{D}_{l'} \mathbf{D}_A \mathbf{D}_\mu \mathbf{H}^{n+\frac{1}{2}}. \end{aligned} \quad (22)$$

The form (22) reveals the physical meaning of the storage function (20a) as a discrete analogy of

$$\frac{1}{2} \iiint_V \varepsilon_x E_x^2 + \varepsilon_y E_y^2 + \varepsilon_z E_z^2 + \mu_x H_x^2 + \mu_y H_y^2 + \mu_z H_z^2 dV \quad (23)$$

For the supply rate, we can substitute (13b) into (20b), obtaining

$$s(\mathbf{y}^n, \mathbf{u}^{n+\frac{1}{2}}) = \Delta t \frac{(\mathbf{x}^n + \mathbf{x}^{n+1})^T}{2} \mathbf{L} \mathbf{L}^T \mathbf{B} \mathbf{u}^{n+\frac{1}{2}}. \quad (24)$$

We show in the Appendix that with the matrix \mathbf{L}^T as in (17), the following condition holds

$$\mathbf{L} \mathbf{L}^T \mathbf{B} = \mathbf{B}, \quad (25)$$

and hence,

$$\begin{aligned} s(\mathbf{y}^n, \mathbf{u}^{n+\frac{1}{2}}) &= \Delta t \frac{(\mathbf{x}^n + \mathbf{x}^{n+1})^T}{2} \mathbf{B} \mathbf{u}^{n+\frac{1}{2}} \\ &= \Delta t \frac{(\mathbf{E}^n + \mathbf{E}^{n+1})^T}{2} \mathbf{D}_l \mathbf{B}_E \mathbf{D}_{l'} \mathbf{u}^{n+\frac{1}{2}}. \end{aligned} \quad (26)$$

The factor $\mathbf{D}_{l'} \mathbf{u}^{n+\frac{1}{2}}$ is a column vector of hanging variables scaled by the lengths of the edges at which they are sampled. Matrix $(\mathbf{E}^n)^T \mathbf{D}_l \mathbf{B}_E$ is a row vector of electric fields corresponding to each of the ports scaled by the lengths of primary edges at which the samples are taken. The sign with which each port contributes to the supply rate is taken according to (12a)–(12c), which is consistent with that of the Poynting vector. As a result, the expression (26) is a discrete version of the integral of Poynting vector over the region boundary from time sample n to $n+1$

$$\int_{n\Delta t}^{(n+1)\Delta t} \oiint_S \vec{E} \times \vec{H} \cdot \hat{\mathbf{n}} dA dt, \quad (27)$$

where $\hat{\mathbf{n}}$ is the unit normal vector.

B. Dissipativity Conditions for the FDTD Region

In [1], we have shown that the system (13a)–(13b) is dissipative if the following conditions hold

$$\mathbf{R} = \mathbf{R}^T > 0, \quad (28a)$$

$$\mathbf{F} + \mathbf{F}^T \geq 0, \quad (28b)$$

$$\mathbf{B} = \mathbf{L} \mathbf{L}^T \mathbf{B}. \quad (28c)$$

Using Schur complement [21], condition (28a) can be written as

$$\mathbf{D}_l \mathbf{D}_{A'} \frac{\mathbf{D}_\varepsilon}{\Delta t} > 0, \quad (29a)$$

$$\mathbf{D}_{l'} \mathbf{D}_A \frac{\mathbf{D}_\mu}{\Delta t} - \frac{\Delta t}{4} \mathbf{D}_{l'} \mathbf{C} \mathbf{D}_l \mathbf{D}_\varepsilon^{-1} \mathbf{D}_{A'}^{-1} \mathbf{C}^T \mathbf{D}_{l'} > 0 \quad (29b)$$

Equation (29a) is true because lengths, areas, and permittivities in the region are positive. By multiplying the left hand side of (29b) by a symmetric matrix $2\mathbf{D}_{l'}^{-\frac{1}{2}} \mathbf{D}_A^{-\frac{1}{2}} \mathbf{D}_\mu^{-\frac{1}{2}} \Delta t^{-\frac{1}{2}}$ from the left and from the right, we can write (29b) as

$$\frac{4}{\Delta t^2} \mathbf{I}_{N_H} - \mathbf{S} \mathbf{S}^T > 0, \quad (30)$$

where

$$\mathbf{S} = \mathbf{D}_A^{-\frac{1}{2}} \mathbf{D}_\mu^{-\frac{1}{2}} \mathbf{D}_{l'}^{\frac{1}{2}} \mathbf{C} \mathbf{D}_l^{\frac{1}{2}} \mathbf{D}_\varepsilon^{-\frac{1}{2}} \mathbf{D}_{A'}^{-\frac{1}{2}}. \quad (31)$$

Condition (30) holds when

$$\Delta t < \min_k \left\{ \frac{2}{s_k} \right\}, \quad (32)$$

where s_k are the non-zero singular values of \mathbf{S} .

Thus, condition (28a) can be seen as a generalized CFL limit. Moreover, with the strategy similar to [4] we can show that the sufficient condition for (28a) to hold is that the classical FDTD CFL limit [3] is met

$$\Delta t < \frac{\sqrt{\mu\varepsilon}}{\sqrt{\frac{1}{\Delta x^2} + \frac{1}{\Delta y^2} + \frac{1}{\Delta z^2}}}, \quad (33)$$

where ε is the smallest primary edge permittivity in the region and μ is the smallest secondary edge permeability. When the CFL limit is violated for any of the cells, the energy stored in that cell is no longer bounded below by zero, which can make the cell capable of supplying unlimited energy to the rest of the system.

Condition (28b) expands into

$$\mathbf{F} + \mathbf{F}^T = \begin{bmatrix} \mathbf{D}_l \mathbf{D}_{A'} \mathbf{D}_\sigma & \mathbf{0} \\ \mathbf{0} & \mathbf{0} \end{bmatrix} \geq 0, \quad (34)$$

which holds when conductivities are non-negative. This ensures that the physical system simulated is dissipative. The third condition (28c) is always true, which is shown in the Appendix.

Thus, FDTD region forms a dissipative dynamical system under the generalized CFL limit and can be arbitrarily interconnected with any other dissipative subsystem without violating stability.

IV. SYSTEMATIC METHOD FOR STABILITY ENFORCEMENT

Suppose we want to construct a stable time-domain system involving one or more FDTD regions and possibly other components connected to the grids, all running at the same time step. With the results of this paper, the task can be accomplished as follows:

- 1) Ports are defined for each block, similarly to the way it is done for FDTD region in Sec. II
- 2) If needed, interpolation rules are created, which are viewed as separate subsystems
- 3) Since 3D FDTD grids are dissipative under their own CFL limits or, more generally, under condition (32), we can prove the stability of the system by ensuring that the rest of the subsystems are dissipative. For dynamical systems of the form (13a)–(13b) this can be done using (28a)–(28c). Alternatively, subsystems that are unable to store energy can be proven dissipative by ensuring that the net supply rate to such subsystem is zero.
- 4) Update scheme is derived such that the equations describing each subsystem, including the interpolation rules, are satisfied. The most restrictive time step is taken to ensure that all subsystems are dissipative.

We demonstrate an application of the method in Sec. V, where we use it to derive a stable subgridding algorithm in 3-D.

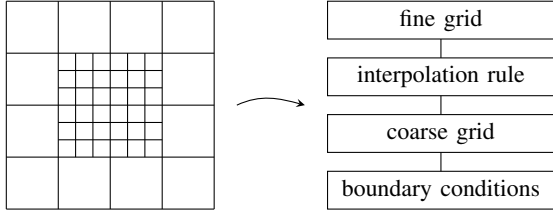


Fig. 3: Illustration of the subgridding scenario. Left: primary grid. Right: subsystem interpretation.

This approach offers substantial simplification to stability enforcement process, because the dissipativity conditions can be imposed on individual subsystems, such as FDTD grids or macromodels [18], as opposed to the entire system. Moreover, this approach allows one to make modifications to parts of the system without re-deriving the entire stability proof for the setup.

It should be noted that, although we use matrix formulation of FDTD equations for proving dissipativity, the final schemes can involve standard FDTD updates for better computational efficiency.

V. APPLICATION TO STABLE 3-D FDTD SUBGRIDDING

Consider a scenario where a fine grid, or subgridding region, is embedded in a coarse grid, as shown in Fig. 3. The fine grid is refined r_x , r_y , and r_z times in x , y , and z directions, respectively, and its boundary coincides with the primary cell boundaries of the coarse grid. The refinement ratios r_x , r_y , and r_z are odd integers larger than 1.

In order to develop a stable subgridding scheme with the method described in Sec. IV, we view this setup as a connection of four subsystems: boundary conditions, the coarse grid, the fine grid, and the interpolation rule that relates inputs and outputs of the two grids, as depicted in Fig. 3.

A. Interpolation Conditions

Consider a portion of the South subgridding boundary, shown in Fig. 4a, extending from $(i - (1/2), j, k)$ to $(i + (1/2), j, k + 1)$ when indexed by the coarse indexes. This corresponds to $(\hat{i}_0 - (r_x/2), 1, \hat{k}_0) \sim (\hat{i}_0 + (r_x/2), 1, \hat{k}_0 + r)$ rectangle on the fine grid's South boundary. For the E_z - U_x pair in the two rectangles we use the following interpolation rules to relate the samples on the fine and coarse sides of the interface. Fine samples are set equal in longitudinal direction over the face shaded in Fig. 4a. In other words, the fine electric field samples \hat{E}_z^n are equal in the z -direction and the finely sampled hanging variables $\hat{U}_x^{n+(1/2)}$ are equal in x -direction

$$\begin{aligned} \hat{E}_z^n|_{\hat{i}, 1, \hat{k}_0 + \frac{1}{2}} &= \hat{E}_z^n|_{\hat{i}, 1, \hat{k}_0 + \frac{3}{2}} = \dots = \hat{E}_z^n|_{\hat{i}, 1, \hat{k}_0 + r - \frac{1}{2}}, \\ \forall \hat{i} &= \hat{i}_0 - \frac{r_x}{2} + \frac{1}{2}, \dots, \hat{i}_0 + \frac{r_x}{2} - \frac{1}{2}, \forall n, \end{aligned} \quad (35a)$$

$$\begin{aligned} \hat{U}_x^{n+\frac{1}{2}}|_{\hat{i}_0 - \frac{r_x}{2} + \frac{1}{2}, 1, \hat{k} + \frac{1}{2}} &= \hat{U}_x^{n+\frac{1}{2}}|_{\hat{i}_0 - \frac{r_x}{2} + \frac{3}{2}, 1, \hat{k} + \frac{1}{2}} \\ &= \dots = \hat{U}_x^{n+\frac{1}{2}}|_{\hat{i}_0 + \frac{r_x}{2} - \frac{1}{2}, 1, \hat{k} + \frac{1}{2}}, \\ \forall \hat{k} &= 1, \dots, \hat{k}_0 + r - 1, \forall n. \end{aligned} \quad (35b)$$

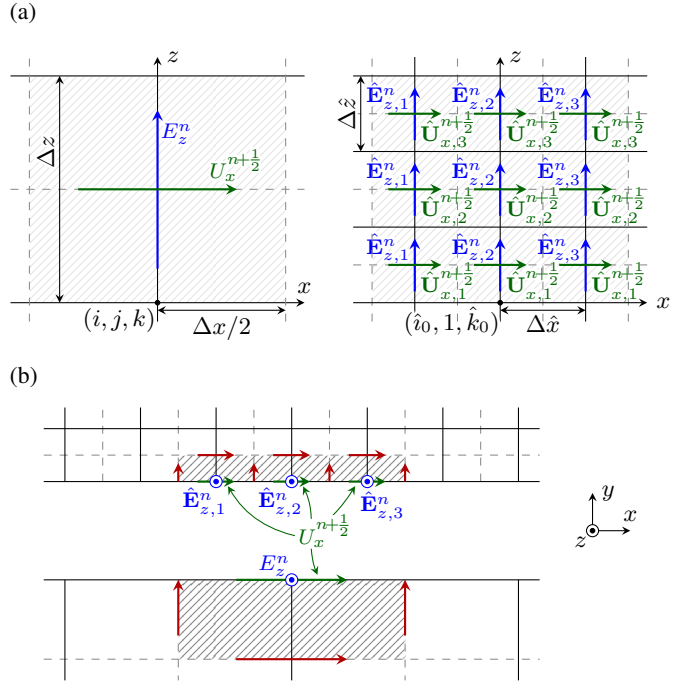


Fig. 4: Coarse and fine sides of the subgridding interface on the South subgridding boundary. (a) Full view of the face over which the interpolation rule applies. (b) 2-D interpretation after the averaging of equations over k has been carried out. Quantities of the form $\hat{\mathbf{E}}_{z,m}^n$ denote m^{th} element of vector $\hat{\mathbf{E}}_z^n$ and similarly for $\hat{\mathbf{U}}_{x,m}^{n+(1/2)}$.

The “ $\hat{\cdot}$ ” notation will henceforth refer to the variables of the subgridding region. For clarity, we switch to the following compact matrix representation, keeping track of the distinct electric and magnetic samples and pruning the redundant variables resulting from (35a)–(35b)

$$\hat{\mathbf{E}}_z^n = \begin{bmatrix} \hat{E}_z^n|_{\hat{i}_0 - \frac{r_x}{2} + \frac{1}{2}, 1, \hat{k}_0 + \frac{1}{2}} \\ \hat{E}_z^n|_{\hat{i}_0 - \frac{r_x}{2} + \frac{3}{2}, 1, \hat{k}_0 + \frac{1}{2}} \\ \vdots \\ \hat{E}_z^n|_{\hat{i}_0 + \frac{r_x}{2} - \frac{1}{2}, 1, \hat{k}_0 + \frac{1}{2}} \end{bmatrix}, \quad \hat{\mathbf{U}}_x^{n+\frac{1}{2}} = \begin{bmatrix} \hat{U}_x^{n+\frac{1}{2}}|_{\hat{i}_0, 1, \hat{k}_0 + \frac{1}{2}} \\ \hat{U}_x^{n+\frac{1}{2}}|_{\hat{i}_0, 1, \hat{k}_0 + \frac{3}{2}} \\ \vdots \\ \hat{U}_x^{n+\frac{1}{2}}|_{\hat{i}_0, 1, \hat{k}_0 + r - \frac{1}{2}} \end{bmatrix}. \quad (36)$$

The coarse electric and magnetic samples are forced to equal the average of fine electric and magnetic samples, respectively

$$E_z^n = \frac{\mathbf{T}_{r_x}^T}{r_x} \hat{\mathbf{E}}_z^n, \quad \forall n, \quad (37a)$$

$$U_x^{n+\frac{1}{2}} = \frac{\mathbf{T}_{r_z}^T}{r_z} \hat{\mathbf{U}}_x^{n+\frac{1}{2}}, \quad \forall n, \quad (37b)$$

where \mathbf{T}_m is an $m \times 1$ matrix of ones and E_z^n and $U_x^{n+(1/2)}$ are the electric and magnetic fields, respectively, sampled coarsely at $(i, j, k + (1/2))$. The other five faces of the subgridding boundary follow interpolation rules analogous to (35a)–(35b) and (37a)–(37b).

Edges of the subgridding boundary are treated similarly, except now two perpendicular faces of the boundary, along with the two sets of hanging variables in two directions

are involved in the interpolation conditions. Consider, for instance, the South-West edge, shown in Fig. 5a. As before, we interpolate the fields located on the shaded portion of the interface so that the fine electric and magnetic field samples are equal in longitudinal directions

$$\hat{E}_z|_{i,j,\hat{k}_0+\frac{1}{2}}^n = \hat{E}_z|_{i,j,\hat{k}_0+\frac{3}{2}}^n = \dots = \hat{E}_z|_{i,j,\hat{k}_0+r_z-\frac{1}{2}}^n, \quad \forall \hat{i} = 1, 2, \dots, \frac{r_x}{2} + \frac{1}{2}, \quad \forall \hat{j} = 1, 2, \dots, \frac{r_y}{2} + \frac{1}{2}, \quad \forall n, \quad (38a)$$

$$\hat{U}_x|_{1,1,\hat{k}+\frac{1}{2}}^{n+\frac{1}{2}} = \hat{U}_x|_{2,1,\hat{k}+\frac{1}{2}}^{n+\frac{1}{2}} = \dots = \hat{U}_x|_{\frac{r_x}{2}+\frac{1}{2},1,\hat{k}+\frac{1}{2}}^{n+\frac{1}{2}}, \quad \forall \hat{k} = \hat{k}_0, \hat{k}_0 + 1, \dots, \hat{k}_0 + r_z - 1, \quad \forall n, \quad (38b)$$

$$\hat{U}_y|_{1,1,\hat{k}+\frac{1}{2}}^{n+\frac{1}{2}} = \hat{U}_y|_{1,2,\hat{k}+\frac{1}{2}}^{n+\frac{1}{2}} = \dots = \hat{U}_y|_{1,\frac{r_y}{2}+\frac{1}{2},\hat{k}+\frac{1}{2}}^{n+\frac{1}{2}}, \quad \forall \hat{k} = \hat{k}_0, \hat{k}_0 + 1, \dots, \hat{k}_0 + r_z - 1, \quad \forall n. \quad (38c)$$

We define the following variables that only keep track of the distinct fine field samples

$$\hat{E}_{zSW}^n = \hat{E}_z|_{1,1,\hat{k}_0+\frac{1}{2}}^n, \quad (39a)$$

$$\hat{\mathbf{E}}_{zW}^n = \left[\hat{E}_z|_{1,2,\hat{k}_0+\frac{1}{2}}^n \quad \dots \quad \hat{E}_z|_{1,\frac{r_y}{2}+\frac{1}{2},\hat{k}_0+\frac{1}{2}}^n \right]^T, \quad (39b)$$

$$\hat{\mathbf{E}}_{zS}^n = \left[\hat{E}_z|_{2,1,\hat{k}_0+\frac{1}{2}}^n \quad \dots \quad \hat{E}_z|_{\frac{r_x}{2}+\frac{1}{2},1,\hat{k}_0+\frac{1}{2}}^n \right]^T, \quad (39c)$$

$$\hat{\mathbf{U}}_x^{n+\frac{1}{2}} = \left[\hat{U}_x|_{1,1,\hat{k}_0+\frac{1}{2}}^{n+\frac{1}{2}} \quad \dots \quad \hat{U}_x|_{1,1,\hat{k}_0+r_z-\frac{1}{2}}^{n+\frac{1}{2}} \right]^T, \quad (39d)$$

$$\hat{\mathbf{U}}_y^{n+\frac{1}{2}} = \left[\hat{U}_y|_{1,1,\hat{k}_0+\frac{1}{2}}^{n+\frac{1}{2}} \quad \dots \quad \hat{U}_y|_{1,1,\hat{k}_0+r_z-\frac{1}{2}}^{n+\frac{1}{2}} \right]^T. \quad (39e)$$

In the case of $r = r_x = r_y = r_z = 3$ as in Fig. 5a, the vectors in (39b) and (39c) reduce to scalars.

Analogously to (37a), we enforce equality of coarse and fine integrals of the z -directed electric field over the West portion of the shaded area in Fig. 5a

$$\frac{\Delta y}{2} E_z^n = \frac{\Delta y}{2r_y} \hat{E}_{zSW}^n + \frac{\Delta y}{r_y} \mathbf{T}_{\frac{r_y}{2}-\frac{1}{2}}^T \hat{\mathbf{E}}_{zW}^n, \quad \forall n. \quad (40a)$$

A similar condition is applied on the South portion

$$\frac{\Delta x}{2} E_z^n = \frac{\Delta x}{2r_x} \hat{E}_{zSW}^n + \frac{\Delta x}{r_x} \mathbf{T}_{\frac{r_x}{2}-\frac{1}{2}}^T \hat{\mathbf{E}}_{zS}^n, \quad \forall n. \quad (40b)$$

The coarse hanging variables are forced to equal the average of the corresponding fine hanging variables

$$U_y^{n+\frac{1}{2}} = \frac{\mathbf{T}_{r_z}^T}{r_z} \hat{\mathbf{U}}_y^{n+\frac{1}{2}}, \quad \forall n, \quad (41a)$$

$$U_x^{n+\frac{1}{2}} = \frac{\mathbf{T}_{r_z}^T}{r_z} \hat{\mathbf{U}}_x^{n+\frac{1}{2}}, \quad \forall n. \quad (41b)$$

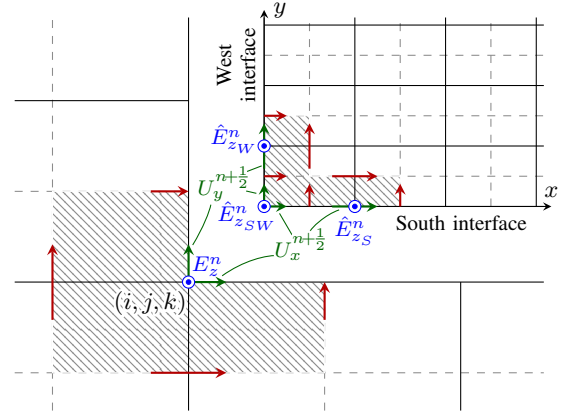
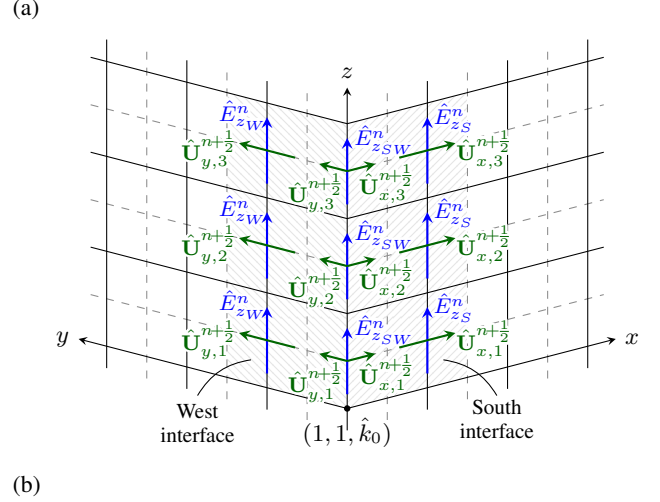


Fig. 5: Illustration of the interpolation rule at the South-Bottom edge of the subgridding boundary. (a) Fine side of the interface. (b) 2-D interpretation after equations have been averaged over \hat{k} .

B. Stability Proof

With the supply rate expression (26), we can easily show that the energy entering the interpolation rule subsystem during a time step is zero. Since (26) is a summation of supply rates associated with each port, or equivalently each hanging variable, it is sufficient to show that the supply rate associated with each x -, y -, and z -directed coarse U -sample balances out the rates associated with the corresponding fine samples. We show that this is the case for U_x component on the South face of the subgridding interface.

Consider the shaded portion of the interface in Fig. 4a. The total supply rate associated with coarse and fine U_x over the two sides of the shaded area can be written as

$$s_{U_x}^{n+\frac{1}{2}} = +\Delta t \Delta x \Delta z \frac{E_z^n + E_z^{n+1}}{2} U_x^{n+\frac{1}{2}} - \Delta t \frac{\Delta x}{r_x} \frac{\Delta z}{r_z} \left(\mathbf{T}_{r_z} \otimes \hat{\mathbf{E}}_z^n + \mathbf{T}_{r_z} \otimes \hat{\mathbf{E}}_z^{n+1} \right)^T \left(\hat{\mathbf{U}}_x^{n+\frac{1}{2}} \otimes \mathbf{T}_{r_x} \right), \quad (42)$$

where \otimes denotes Kronecker product [22], which is used to retrieve the complete vectors of electric and magnetic field

samples from the compact vectors in (36). Using the properties of the Kronecker product [22], we can rewrite (42) as

$$s_{U_x}^{n+\frac{1}{2}} = +\Delta t \Delta x \Delta z \frac{E_z^n + E_z^{n+1}}{2} U_x^{n+\frac{1}{2}} - \Delta t \frac{\Delta x}{r_x} \frac{\Delta z}{r_z} \mathbf{T}_{r_z}^T \hat{\mathbf{U}}_x^{n+\frac{1}{2}} \frac{(\hat{\mathbf{E}}_z^n + \hat{\mathbf{E}}_z^{n+1})^T}{2} \mathbf{T}_{r_x}. \quad (43)$$

Substituting (37a) and (37b) into (43), we obtain

$$s_{U_x}^{n+\frac{1}{2}} = +\Delta t \Delta x \Delta z \frac{E_z^n + E_z^{n+1}}{2} U_x^{n+\frac{1}{2}} - \Delta t \frac{\Delta x}{r_x} \frac{\Delta z}{r_z} r_z U_x^{n+\frac{1}{2}} \frac{(r_x E_z^n + r_x E_z^{n+1})^T}{2} = 0. \quad (44)$$

Likewise, consider the South portion of the shaded area in Fig. 5a, which shows a West-most coarse half-face on the South subgridding boundary. For this half-face, the contribution of ports associated with x -directed hanging variables to the supply rate is

$$s_{U_x}^{n+\frac{1}{2}} = +\Delta t \frac{\Delta x}{2} \Delta z \frac{E_z^n + E_z^{n+\frac{1}{2}}}{2} U_x^{n+\frac{1}{2}} - \Delta t \frac{\Delta x}{r_x} \frac{\Delta z}{r_z} \mathbf{T}_{r_z}^T \hat{\mathbf{U}}_x^{n+\frac{1}{2}} \frac{(\hat{\mathbf{E}}_{z_S}^n + \hat{\mathbf{E}}_{z_S}^{n+1})^T}{2} \mathbf{T}_{r_x - \frac{1}{2}} - \Delta t \frac{\Delta x}{2r_x} \frac{\Delta z}{r_z} \mathbf{T}_{r_z}^T \hat{\mathbf{U}}_x^{n+\frac{1}{2}} \frac{\hat{E}_{z_{SW}}^n + \hat{E}_{z_{SW}}^{n+\frac{1}{2}}}{2}, \quad (45)$$

where $\hat{E}_{z_{SW}}^n$, $\hat{\mathbf{E}}_{z_S}^n$, and $\hat{\mathbf{U}}_x^{n+\frac{1}{2}}$ are defined in (39a), (39c), and (39d), respectively. Substituting (41b), equation (45) becomes

$$s_{U_x}^{n+\frac{1}{2}} = +\Delta t \frac{\Delta x}{2} \Delta z \frac{E_z^n + E_z^{n+\frac{1}{2}}}{2} U_x^{n+\frac{1}{2}} - \Delta t \frac{\Delta z}{r_z} r_z U_x^{n+\frac{1}{2}} \times \left(\frac{\Delta x}{r_x} \frac{(\hat{\mathbf{E}}_{z_S}^n + \hat{\mathbf{E}}_{z_S}^{n+1})^T}{2} \mathbf{T}_{r_x - \frac{1}{2}} + \frac{\Delta x}{2r_x} \frac{\hat{E}_{z_{SW}}^n + \hat{E}_{z_{SW}}^{n+\frac{1}{2}}}{2} \right), \quad (46)$$

which is zero because of (40b).

With a similar argument, we can show that the supply rate due to U_x on the East-most half-faces of the South subgridding boundary equals zero. The same is true for the net contributions of all other boundary ports. This means that the total power leaving the fine grid is equal to the power that the interpolation rule supplies to the coarse grid. This makes the interpolation rule a lossless, and hence dissipative, subsystem. Since the coarse and fine grids are dissipative under their own CFL limits, the entire scheme is stable under the CFL limit of the fine grid, which is the most restrictive CFL limit.

C. Practical Implementation

Interpolation conditions defined in Sec. V-A can now be used to derive update equations for the coarse and fine electric field samples on the interface between the two regions. Referring to Fig. 4a, the fine electric field samples at each fine node $(\hat{i}, 1, \hat{k} + (1/2))$ in the range from $(\hat{i}_0 - r_x/2 +$

$(1/2), 1, \hat{k}_0 + (1/2))$ to $(\hat{i}_0 + r_x/2 - (1/2), 1, \hat{k}_0 + r_z - (1/2))$ satisfy the following equations

$$\begin{aligned} & \frac{\Delta x}{r_x} \frac{\Delta y}{2r_y} \left(\frac{\hat{\varepsilon}_z|_{\hat{i},1,\hat{k}+\frac{1}{2}}}{\Delta t} + \frac{\hat{\sigma}_z|_{\hat{i},1,\hat{k}+\frac{1}{2}}}{2} \right) \hat{E}_z|_{\hat{i},1,\hat{k}_0+\frac{1}{2}}^{n+1} \\ &= \frac{\Delta x}{r_x} \frac{\Delta y}{2r_y} \left(\frac{\hat{\varepsilon}_z|_{\hat{i},1,\hat{k}+\frac{1}{2}}}{\Delta t} - \frac{\hat{\sigma}_z|_{\hat{i},1,\hat{k}+\frac{1}{2}}}{2} \right) \hat{E}_z|_{\hat{i},1,\hat{k}_0+\frac{1}{2}}^n \\ & \quad - \frac{\Delta x}{r_x} \hat{H}_x|_{\hat{i},\frac{3}{2},\hat{k}+\frac{1}{2}}^{n+\frac{1}{2}} - \frac{\Delta y}{2r_y} \hat{H}_y|_{\hat{i}-\frac{1}{2},1,\hat{k}+\frac{1}{2}}^{n+\frac{1}{2}} \\ & \quad + \frac{\Delta y}{2r_y} \hat{H}_y|_{\hat{i}+\frac{1}{2},1,\hat{k}+\frac{1}{2}}^{n+\frac{1}{2}} + \frac{\Delta x}{r_x} \hat{U}_x|_{\hat{i}_0,1,\hat{k}+\frac{1}{2}}^{n+\frac{1}{2}}. \end{aligned} \quad (47)$$

Using (35a) and averaging (47) over \hat{k} indexes in the shaded area we obtain the following equation for each $\hat{E}_z|_{\hat{i},1,\hat{k}_0+(1/2)}^n$

$$\begin{aligned} & \frac{\Delta x}{r_x} \frac{\Delta y}{2r_y} \frac{1}{r_z} \sum_{\hat{k}=\hat{k}_0}^{\hat{k}_0+r_z-1} \left\{ \frac{\hat{\varepsilon}_z|_{\hat{i},1,\hat{k}+\frac{1}{2}}}{\Delta t} + \frac{\hat{\sigma}_z|_{\hat{i},1,\hat{k}+\frac{1}{2}}}{2} \right\} \hat{E}_z|_{\hat{i},1,\hat{k}_0+\frac{1}{2}}^{n+1} \\ &= \frac{\Delta x}{r_x} \frac{\Delta y}{2r_y} \frac{1}{r_z} \sum_{\hat{k}=\hat{k}}^{\hat{k}_0+r_z-1} \left\{ \frac{\hat{\varepsilon}_z|_{\hat{i},1,\hat{k}+\frac{1}{2}}}{\Delta t} - \frac{\hat{\sigma}_z|_{\hat{i},1,\hat{k}+\frac{1}{2}}}{2} \right\} \hat{E}_z|_{\hat{i},1,\hat{k}+\frac{1}{2}}^n \\ & \quad - \frac{\Delta x}{r_x} \frac{1}{r_z} \sum_{\hat{k}=\hat{k}_0}^{\hat{k}_0+r_z-1} \hat{H}_x|_{\hat{i},\frac{3}{2},\hat{k}+\frac{1}{2}}^{n+\frac{1}{2}} - \frac{\Delta y}{2r_y} \frac{1}{r_z} \sum_{\hat{k}=\hat{k}_0}^{\hat{k}_0+r_z-1} \hat{H}_y|_{\hat{i}-\frac{1}{2},1,\hat{k}+\frac{1}{2}}^{n+\frac{1}{2}} \\ & \quad + \frac{\Delta y}{2r_y} \frac{1}{r_z} \sum_{\hat{k}=\hat{k}_0}^{\hat{k}_0+r_z-1} \hat{H}_y|_{\hat{i}+\frac{1}{2},1,\hat{k}+\frac{1}{2}}^{n+\frac{1}{2}} + \frac{\Delta x}{r_x} \frac{1}{r_z} \sum_{\hat{k}=\hat{k}_0}^{\hat{k}_0+r_z-1} \hat{U}_x|_{\hat{i}_0,1,\hat{k}+\frac{1}{2}}^{n+\frac{1}{2}}. \end{aligned} \quad (48)$$

Using (37b) we can simplify the averages of fine hanging variables in (48) with $U_x^{n+(1/2)}$, which yields the following relation for \mathbf{E}^n vector, written in matrix form

$$\begin{aligned} & \frac{\Delta x}{r_x} \frac{\Delta y}{2r_y} \left(\frac{\hat{\mathbf{D}}_{\varepsilon_z}}{\Delta t} + \frac{\hat{\mathbf{D}}_{\sigma_z}}{2} \right) \hat{\mathbf{E}}_z^{n+1} \\ &= \frac{\Delta x}{r_x} \frac{\Delta y}{2r_y} \left(\frac{\hat{\mathbf{D}}_{\varepsilon_z}}{\Delta t} - \frac{\hat{\mathbf{D}}_{\sigma_z}}{2} \right) \hat{\mathbf{E}}_z^n - \frac{\Delta x}{r_x} \hat{\mathbf{H}}_x^{n+\frac{1}{2}} \\ & \quad - \frac{\Delta y}{2r_y} \hat{\mathbf{H}}_{y,\hat{i}-\frac{1}{2}}^{n+\frac{1}{2}} + \frac{\Delta y}{2r_y} \hat{\mathbf{H}}_{y,\hat{i}+\frac{1}{2}}^{n+\frac{1}{2}} + \frac{\Delta x}{r_x} \mathbf{T}_{r_x} U_x^{n+\frac{1}{2}}, \end{aligned} \quad (49)$$

where $\hat{\mathbf{E}}_z^n$ and $\hat{\mathbf{U}}_x$ are defined in (36), and

$$\hat{\mathbf{H}}_x^{n+\frac{1}{2}} = \begin{bmatrix} \frac{1}{r_z} \sum_{\hat{k}=\hat{k}_0}^{\hat{k}_0+r_z-1} \hat{H}_x|_{\hat{i}_0-\frac{r_x}{2}+\frac{1}{2},\frac{3}{2},\hat{k}+\frac{1}{2}}^{n+\frac{1}{2}} \\ \vdots \\ \frac{1}{r_z} \sum_{\hat{k}=\hat{k}_0}^{\hat{k}_0+r_z-1} \hat{H}_x|_{\hat{i}_0+\frac{r_x}{2}-\frac{1}{2},\frac{3}{2},\hat{k}+\frac{1}{2}}^{n+\frac{1}{2}} \end{bmatrix}, \quad (50a)$$

$$\hat{\mathbf{H}}_{y,\hat{i}-\frac{1}{2}}^{n+\frac{1}{2}} = \begin{bmatrix} \frac{1}{r_z} \sum_{\hat{k}=\hat{k}_0}^{\hat{k}_0+r_z-1} \hat{H}_y|_{\hat{i}_0-\frac{r_x}{2},1,\hat{k}+\frac{1}{2}}^{n+\frac{1}{2}} \\ \vdots \\ \frac{1}{r_z} \sum_{\hat{k}=\hat{k}_0}^{\hat{k}_0+r_z-1} \hat{H}_y|_{\hat{i}_0+\frac{r_x}{2}-1,1,\hat{k}+\frac{1}{2}}^{n+\frac{1}{2}} \end{bmatrix}, \quad (50b)$$

$$\hat{\mathbf{H}}_{y,\hat{i}+\frac{1}{2}}^{n+\frac{1}{2}} = \begin{bmatrix} \frac{1}{r_z} \sum_{\hat{k}=\hat{k}_0}^{\hat{k}_0+r_z-1} \hat{H}_y|_{\hat{i}_0-\frac{r_x}{2}+1,1,\hat{k}+\frac{1}{2}}^{n+\frac{1}{2}} \\ \vdots \\ \frac{1}{r_z} \sum_{\hat{k}=\hat{k}_0}^{\hat{k}_0+r_z-1} \hat{H}_y|_{\hat{i}_0+\frac{r_x}{2},1,\hat{k}+\frac{1}{2}}^{n+\frac{1}{2}} \end{bmatrix}. \quad (50c)$$

Diagonal matrix $\hat{\mathbf{D}}_{\varepsilon_z}$ in (49) contains permittivities on the fine grid's side, averaged over z -directed lines at $\hat{i} = \hat{i}_0 - \frac{r_x}{2} + \frac{1}{2}$ through $\hat{i} = \hat{i}_0 + \frac{r_x}{2} - \frac{1}{2}$. Conductivity matrix $\hat{\mathbf{D}}_{\sigma_z}$ is defined analogously.

The coarse field E_z^n needs to satisfy

$$\begin{aligned} \Delta x \frac{\Delta y}{2} \left(\frac{\varepsilon_z}{\Delta t} + \frac{\sigma_z}{2} \right) E_z^{n+1} &= \Delta x \frac{\Delta y}{2} \left(\frac{\varepsilon_z}{\Delta t} - \frac{\sigma_z}{2} \right) E_z^n + \Delta x H_x|_{j-\frac{1}{2}}^{n+\frac{1}{2}} \\ &\quad - \frac{\Delta y}{2} H_y|_{i-\frac{1}{2}}^{n+\frac{1}{2}} + \frac{\Delta y}{2} H_y|_{i+\frac{1}{2}}^{n+\frac{1}{2}} - \Delta x U_x^{n+\frac{1}{2}}, \end{aligned} \quad (51)$$

where subscripts i , j , and $k + (1/2)$ are dropped for clarity.

Virtually, the task of deriving the update equation changes to a 2-D problem, as illustrated in Fig. 4b, where the unknowns, E_z^{n+1} and $\hat{\mathbf{E}}_z^{n+1}$, need to simultaneously satisfy (49) and (51), along with the interpolation condition on E in (37a).

Substituting (37a) into (51) and multiplying the result on the left by \mathbf{T}_{r_x}/r_x , we obtain

$$\begin{aligned} \Delta x \frac{\Delta y}{2} \left(\frac{\varepsilon_z}{\Delta t} + \frac{\sigma_z}{2} \right) \frac{\mathbf{1}_{r_x}}{r_x^2} \hat{\mathbf{E}}_z^{n+1} &= \Delta x \frac{\Delta y}{2} \left(\frac{\varepsilon_z}{\Delta t} - \frac{\sigma_z}{2} \right) \frac{\mathbf{1}_{r_x}}{r_x^2} \hat{\mathbf{E}}_z^n + \Delta x \frac{\mathbf{T}_{r_x}}{r_x} H_x|_{j-\frac{1}{2}}^{n+\frac{1}{2}} \\ &\quad - \frac{\Delta y}{2} \frac{\mathbf{T}_{r_x}}{r_x} H_y|_{i-\frac{1}{2}}^{n+\frac{1}{2}} + \frac{\Delta y}{2} \frac{\mathbf{T}_{r_x}}{r_x} H_y|_{i+\frac{1}{2}}^{n+\frac{1}{2}} - \Delta x \frac{\mathbf{T}_{r_x}}{r_x} U_x^{n+\frac{1}{2}}, \end{aligned} \quad (52)$$

where $\mathbf{1}$ denotes a square matrix of ones with the subscript denoting its size. Adding (49) to (52) yields

$$\begin{aligned} &\left[\Delta x \frac{\Delta y}{2} \left(\frac{\varepsilon_z}{\Delta t} + \frac{\sigma_z}{2} \right) \frac{\mathbf{1}_{r_x}}{r_x^2} + \frac{\Delta x}{r_x} \frac{\Delta y}{2 r_y} \left(\hat{\mathbf{D}}_{\varepsilon_z} + \frac{\hat{\mathbf{D}}_{\sigma_z}}{2} \right) \right] \hat{\mathbf{E}}_z^{n+1} \\ &= \left[\Delta x \frac{\Delta y}{2} \left(\frac{\varepsilon_z}{\Delta t} - \frac{\sigma_z}{2} \right) \frac{\mathbf{1}_x}{r_x^2} + \frac{\Delta x}{r_x} \frac{\Delta y}{2 r_y} \left(\hat{\mathbf{D}}_{\varepsilon_z} - \frac{\hat{\mathbf{D}}_{\sigma_z}}{2} \right) \right] \hat{\mathbf{E}}_z^n \\ &\quad + \Delta x \frac{\mathbf{T}_{r_x}}{r_x} H_x|_{j-\frac{1}{2}}^{n+\frac{1}{2}} - \frac{\Delta y}{2} \frac{\mathbf{T}_{r_x}}{r_x} H_y|_{i-\frac{1}{2}}^{n+\frac{1}{2}} + \frac{\Delta y}{2} \frac{\mathbf{T}_{r_x}}{r_x} H_y|_{i+\frac{1}{2}}^{n+\frac{1}{2}} \\ &\quad - \frac{\Delta x}{r_x} \hat{\mathbf{H}}_x^{n+\frac{1}{2}} - \frac{\Delta y}{2 r_y} \hat{\mathbf{H}}_{y,\hat{i}-\frac{1}{2}}^{n+\frac{1}{2}} + \frac{\Delta y}{2 r_y} \hat{\mathbf{H}}_{y,\hat{i}+\frac{1}{2}}^{n+\frac{1}{2}}. \end{aligned} \quad (53)$$

Multiplying the equation by the inverse of the coefficient in front of $\hat{\mathbf{E}}_z^{n+1}$, we obtain an explicit update equation for the distinct fine electric fields in the shaded region in Fig. 4a. The rest of fine fields in that region can be updated using the equality (35a) and the coarse electric field sample is updated using (37a).

The update equations for electric fields of Type II are derived using the modified FDTD equations on each side of the interface and the interpolation conditions (38a)–(38c), (40a)–(40b), and (41b)–(41a). Referring to Fig. 5a, the coarse E -field

at (i, j, k) node needs to satisfy the modified FDTD equation

$$\begin{aligned} &3 \frac{\Delta x}{2} \frac{\Delta y}{2} \left(\frac{\varepsilon_z}{\Delta t} + \frac{\sigma_z}{2} \right) E_z^{n+1} \\ &= 3 \frac{\Delta x}{2} \frac{\Delta y}{2} \left(\frac{\varepsilon_z}{\Delta t} - \frac{\sigma_z}{2} \right) E_z^n - \frac{\Delta x}{2} H_x|_{j+\frac{1}{2}}^{n+\frac{1}{2}} \\ &\quad + \Delta x H_x|_{j-\frac{1}{2}}^{n+\frac{1}{2}} - \Delta y H_y|_{i-\frac{1}{2}}^{n+\frac{1}{2}} + \frac{\Delta y}{2} H_y|_{i+\frac{1}{2}}^{n+\frac{1}{2}} \\ &\quad - \frac{\Delta x}{2} U_x^{n+\frac{1}{2}} + \frac{\Delta y}{2} U_y^{n+\frac{1}{2}}. \end{aligned} \quad (54)$$

Applying a similar averaging procedure as was used for the fields of Type I, we obtain the following equations for the distinct fine electric fields defined in (39a)–(39c)

$$\begin{aligned} &\frac{\Delta x}{2 r_x} \frac{\Delta y}{2 r_y} \left(\frac{\hat{\varepsilon}_{zsw}}{\Delta t} + \frac{\hat{\sigma}_{zsw}}{2} \right) \hat{E}_{zsw}^{n+1} \\ &= \frac{\Delta x}{2 r_x} \frac{\Delta y}{2 r_y} \left(\frac{\hat{\varepsilon}_{zsw}}{\Delta t} - \frac{\hat{\sigma}_{zsw}}{2} \right) \hat{E}_{zsw}^n - \frac{\Delta x}{2 r_x} \hat{H}_x|_{W,j=\frac{3}{2}}^{n+\frac{1}{2}} \\ &\quad + \frac{\Delta y}{2 r_y} \hat{H}_y|_{S,\hat{i}=\frac{3}{2}}^{n+\frac{1}{2}} + \frac{\Delta x}{2 r_x} U_x^{n+\frac{1}{2}} - \frac{\Delta y}{2 r_y} U_y^{n+\frac{1}{2}}, \end{aligned} \quad (55a)$$

$$\begin{aligned} &\frac{\Delta x}{2 r_x} \frac{\Delta y}{r_y} \left(\frac{\hat{\mathbf{D}}_{\varepsilon_{zw}}}{\Delta t} + \frac{\hat{\mathbf{D}}_{\sigma_{zw}}}{2} \right) \hat{\mathbf{E}}_{zw}^{n+1} \\ &= \frac{\Delta x}{2 r_x} \frac{\Delta y}{r_y} \left(\frac{\hat{\mathbf{D}}_{\varepsilon_{zw}}}{\Delta t} - \frac{\hat{\mathbf{D}}_{\sigma_{zw}}}{2} \right) \hat{\mathbf{E}}_{zw}^n + \frac{\Delta x}{2 r_x} \hat{\mathbf{H}}_{x,W,j=\frac{1}{2}}^{n+\frac{1}{2}} \\ &\quad - \frac{\Delta x}{2 r_x} \hat{\mathbf{H}}_{x,W,j+\frac{1}{2}}^{n+\frac{1}{2}} + \frac{\Delta y}{r_y} \hat{\mathbf{H}}_{y,\hat{i}=\frac{3}{2}}^{n+\frac{1}{2}} - \frac{\Delta y}{r_y} \mathbf{T}_{\frac{r_y}{2}-\frac{1}{2}} U_y^{n+\frac{1}{2}}, \end{aligned} \quad (55b)$$

$$\begin{aligned} &\frac{\Delta x}{r_x} \frac{\Delta y}{2 r_y} \left(\frac{\hat{\mathbf{D}}_{\varepsilon_{zs}}}{\Delta t} + \frac{\hat{\mathbf{D}}_{\sigma_{zs}}}{2} \right) \hat{\mathbf{E}}_{zs}^{n+1} \\ &= \frac{\Delta x}{r_x} \frac{\Delta y}{2 r_y} \left(\frac{\hat{\mathbf{D}}_{\varepsilon_{zs}}}{\Delta t} - \frac{\hat{\mathbf{D}}_{\sigma_{zs}}}{2} \right) \hat{\mathbf{E}}_{zs}^n - \frac{\Delta x}{r_x} \hat{\mathbf{H}}_{x,j=\frac{3}{2}}^{n+\frac{1}{2}} \\ &\quad - \frac{\Delta y}{2 r_y} \hat{\mathbf{H}}_{y,S,\hat{i}-\frac{1}{2}}^{n+\frac{1}{2}} + \frac{\Delta y}{2 r_y} \hat{\mathbf{H}}_{y,S,\hat{i}+\frac{1}{2}}^{n+\frac{1}{2}} + \frac{\Delta x}{r_x} \mathbf{T}_{\frac{r_x}{2}-\frac{1}{2}} \hat{U}_x^{n+\frac{1}{2}}, \end{aligned} \quad (55c)$$

where

$$\hat{H}_x|_{W,j=\frac{3}{2}}^{n+\frac{1}{2}} = \frac{1}{r_z} \sum_{\hat{k}=\hat{k}_0}^{\hat{k}_0+r_z-1} \hat{H}_x|_{1,\frac{3}{2},\hat{k}+\frac{1}{2}}^{n+\frac{1}{2}}, \quad (56a)$$

$$\hat{\mathbf{H}}_{x,W,j-\frac{1}{2}}^{n+\frac{1}{2}} = \begin{bmatrix} \frac{1}{r_z} \sum_{\hat{k}=\hat{k}_0}^{\hat{k}_0+r_z-1} \hat{H}_x|_{1,\frac{1}{2},\hat{k}+\frac{1}{2}}^{n+\frac{1}{2}} \\ \vdots \\ \frac{1}{r_z} \sum_{\hat{k}=\hat{k}_0}^{\hat{k}_0+r_z-1} \hat{H}_x|_{1,\frac{r_y}{2},\hat{k}+\frac{1}{2}}^{n+\frac{1}{2}} \end{bmatrix}, \quad (56b)$$

$$\hat{\mathbf{H}}_{x,W,j+\frac{1}{2}}^{n+\frac{1}{2}} = \begin{bmatrix} \frac{1}{r_z} \sum_{\hat{k}=\hat{k}_0}^{\hat{k}_0+r_z-1} \hat{H}_x|_{1,\frac{3}{2},\hat{k}+\frac{1}{2}}^{n+\frac{1}{2}} \\ \vdots \\ \frac{1}{r_z} \sum_{\hat{k}=\hat{k}_0}^{\hat{k}_0+r_z-1} \hat{H}_x|_{1,1+\frac{r_y}{2},\hat{k}+\frac{1}{2}}^{n+\frac{1}{2}} \end{bmatrix}, \quad (56c)$$

$$\hat{\mathbf{H}}_{x,\hat{j}=\frac{3}{2}}^{n+\frac{1}{2}} = \begin{bmatrix} \frac{1}{r_z} \sum_{\hat{k}=\hat{k}_0}^{\hat{k}_0+r_z-1} \hat{H}_x|_{2,\frac{3}{2},\hat{k}+\frac{1}{2}}^{n+\frac{1}{2}} \\ \vdots \\ \frac{1}{r_z} \sum_{\hat{k}=\hat{k}_0}^{\hat{k}_0+r_z-1} \hat{H}_x|_{\frac{r_x}{2}+\frac{1}{2},\frac{3}{2},\hat{k}+\frac{1}{2}}^{n+\frac{1}{2}} \end{bmatrix}, \quad (56d)$$

and similarly for $\hat{H}_y|_{S,\hat{i}=3/2}^{n+(1/2)}$, $\hat{\mathbf{H}}_{y,S,\hat{i}-(1/2)}^{n+(1/2)}$, $\hat{\mathbf{H}}_{y,S,\hat{i}+(1/2)}^{n+(1/2)}$, and $\hat{\mathbf{H}}_{y,\hat{i}=3/2}^{n+(1/2)}$. Permittivity and conductivity matrices contain the values averaged over \hat{k} from $\hat{k}_0 + \frac{1}{2}$ to $\hat{k}_0 + r_z - \frac{1}{2}$.

From equations (54), (55a)–(55c), and (40a)–(40b), we obtain a linear system of the form

$$\mathbf{A}\mathbf{z} = \mathbf{b}, \quad (57)$$

with an $(r_x/2 + r_y/2 + 3) \times 1$ vector of unknowns

$$\mathbf{z} = \begin{bmatrix} E_z^{n+1} \\ \hat{E}_{z_{SW}}^{n+1} \\ \hat{E}_{z_W}^{n+1} \\ \hat{E}_{z_S}^{n+1} \\ U_x^{n+\frac{1}{2}} \\ U_y^{n+\frac{1}{2}} \end{bmatrix}. \quad (58)$$

Solving (57) for \mathbf{z} gives values of E_z^{n+1} , $\hat{E}_{z_{SW}}^{n+1}$, $\hat{E}_{z_W}^{n+1}$, and $\hat{E}_{z_S}^{n+1}$, which allows updating all electric fields in the shaded region in Fig. 5a. The same is done on the other seven edges of the boundary of the subgridding region.

We use the following procedure to update the field samples in the system.

- 1) Starting with E^n and $H^{n+(1/2)}$, we update all electric fields strictly inside fine and coarse regions using standard FDTD equations.
- 2) We update electric fields on the interface between the two grids using the special update equations derived above.
- 3) All standard magnetic field samples are updated using standard FDTD update equations to obtain their values at $n + \frac{3}{2}$.

The procedure does not incur significant computational overhead because the the interface samples are updated using either the equations similar in structure to FDTD equations, or by solving very small $\mathcal{O}(r)$ -sized systems for updating fields of Type II. The inclusion of material properties rigorously guarantees stability in the case when arbitrary permittivities and conductivities are assigned to cells on each side of the subgridding interface, in contrast to many of the existing schemes with material traverse where stability could only be verified numerically [23], [24].

VI. NUMERICAL EXAMPLES

The subgridding algorithm from Sec. V was implemented in MATLAB in order to test the validity of the proposed theory for FDTD stability and to assess the accuracy of the proposed subgridding method. The time-consuming portions of the code, such as the update equations for the fields inside each grid, were written using vectorized operations.

A. Stability Verification

We verify the stability of the algorithm by simulating the subgridding scenario shown in Fig. 6 for a million time steps. The setup consists of a 12 cm \times 12 cm \times 12 cm cavity with perfect electric conductor (PEC) as the boundary condition. The grid is discretized with 1 cm mesh and a 4 cm \times 4 cm

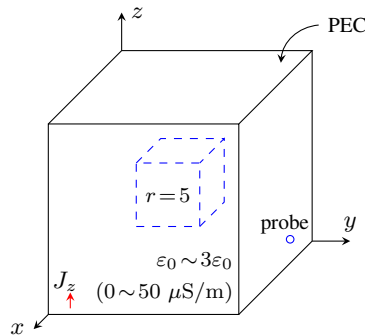


Fig. 6: Setup of the stability verification test in Sec. VI-A.

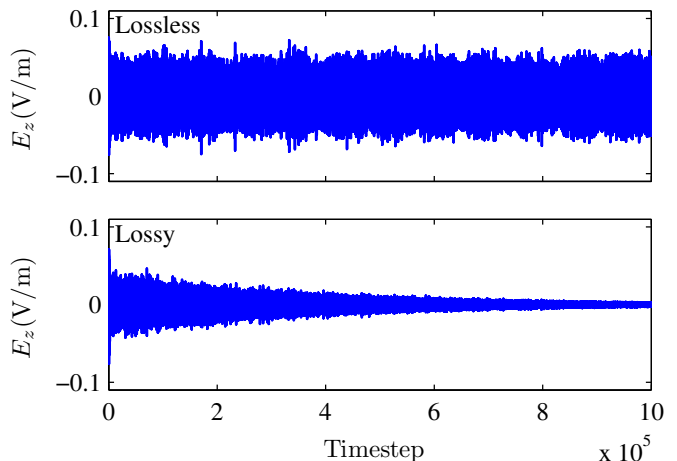


Fig. 7: z component of electric field at the probe in the stability verification test of Sec. VI-A.

\times 4 cm subgridding region with refinement ratio $r = 5$ in all directions is placed at the center of the cavity. Time step is set to 99% of the fine grid's CFL limit. We excite the cavity using a Gaussian pulse with half-width at half-maximum bandwidth of 3.53 GHz.

In order to ensure the correctness of stability analysis in the case when material properties vary, we randomly assign permittivity values to cells in both grids between the free space value ϵ_0 and $3\epsilon_0$ using *rand()* function in MATLAB. Handling of losses is verified by introducing random conductivities between zero and 5×10^{-5} S/m.

From the results, presented in Fig. 7, it can be seen that no signs of instability occur during the million time steps of the simulation. This validates the correctness of the stability analysis framework presented in this paper.

B. Material Traverse

In this simulation we test whether the proposed subgridding method produces consistent results when the subgridding interface traverses material boundaries, which is known to be a challenging scenario for subgridding schemes. We use the setup shown in Fig. 8, where the subgridding region is placed in two different ways such that one of the faces of the grid interface traverses a block of material. As a reference, we run

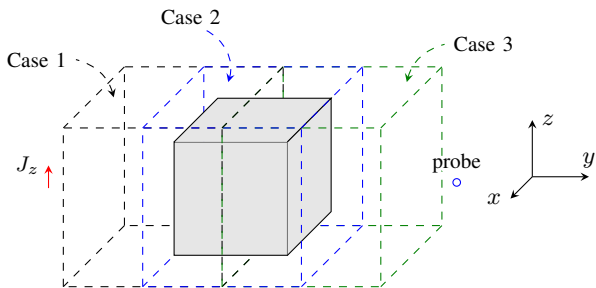


Fig. 8: Setup of the material traverse test from Sec. VI-B.

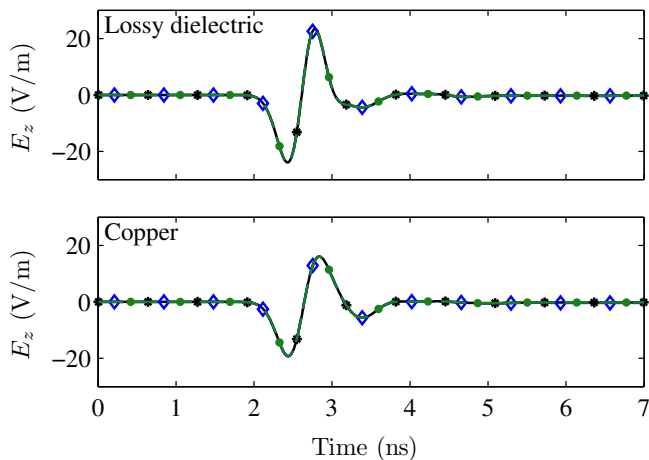


Fig. 9: z component of electric field at the probe in material traverse test in Sec. VI-B for Case 1 ($-*$), Case 2 ($-\diamond-$), and Case 3 ($-\bullet-$).

a simulation where the block is fully enclosed by the subgridding region. The coarse grid is set to $\Delta x = \Delta y = \Delta z = 1$ cm and the subgridding region is refined by a factor of $r = 3$ in each direction. We perform the test for a copper block and for a block with relative permittivity of 3 and conductivity of 0.05 S/m. Gaussian source waveform with half width at half maximum bandwidth of 1.02 GHz is used. The iteration time step is 1% below the CFL limit of the fine grid.

Fig. 9 shows the electric field recorded at the probe in the simulations above. The two cases with material traverse are in very good agreement with the reference simulation. The test was successful for both lossy dielectric and for copper.

C. Meta-screen

In this example we use subgridding to study the three-slot meta-screen shown in Fig. 10. The setup for this simulation is similar to [25], except for differences in discretization and screen material. In particular, we set the plate conductivity to 1.3×10^6 S/m and thickness of the plate to 6 mils, based on the value in [26]. The slot in the center is 13.2 mm by 1.2 mm and the two satellite slots on the sides are 17 mm by 0.6 mm, placed at a center-to-center distance of 3 mm away from the central slot. These dimensions were designed to achieve subwavelength focusing at 10 GHz [26]. We place a line of probes 4.572 mm from the meta-screen, which corresponds to

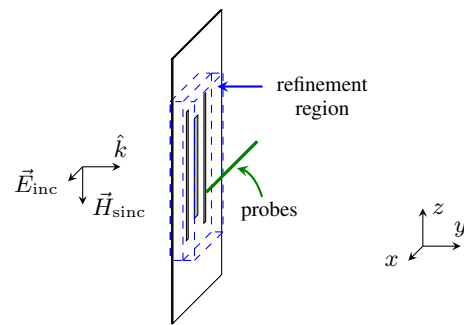


Fig. 10: Setup of the meta-screen example in Sec. VI-C.

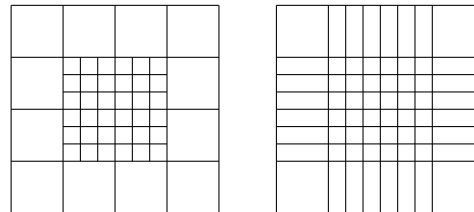


Fig. 11: Schematic representation of the difference between subgridding and refinement using a non-uniform grid.

approximately 15% of the wavelength at 10 GHz – distance at which measurements were performed in [26].

The satellite slots have widths of only 2% of the wavelength, which makes the problem intrinsically multiscale. Moreover, [25] report resonance effects that make it difficult to resolve the structure near the design frequency. We choose this example to investigate the performance of the proposed subgridding scheme.

In order to provide good resolution, we set the fine grid to have $\Delta \hat{x} = 0.1$ mm, $\Delta \hat{y} = 0.0508$ mm, and $\Delta \hat{z} = 0.1$ mm. Because of the large size of simulation volume (25.2 mm \times 19.5072 mm \times 43.4 mm including PML) the use of the fine grid throughout the simulation domain would be prohibitive. Instead, we make $\Delta x = 0.7$ mm, $\Delta y = 0.1524$ mm, and $\Delta z = 0.7$ mm in the main simulation volume by means of subgridding. As a reference, we perform a conventional FDTD simulation with nonuniform grid, schematically shown in Fig. 11. We also simulate the case where the entire grid is discretized with the coarse 0.7 mm \times 0.1524 mm \times 0.7 mm mesh. Proposed method and non-uniform discretization test are run at $\Delta t = 0.1362$ ps, whereas the coarse grid simulation has the iteration time step of 0.4810 ps. The waveform is recorded for 5.5 ns, as in [25].

Fig. 12 shows the amplitude of the x component of the electric field at 10 GHz, which was obtained by Fourier transform from the time-domain waveforms. The results from subgridding are in very good agreement with the reference simulation. In contrast, the coarse resolution was insufficient to perform accurate simulation of the meta-screen. This is not surprising, since any mesh with Δx larger than 0.3 mm or Δz larger than 0.1 mm cannot correctly resolve the meta-screen structure, let alone the fields around the slots.

The simulation times, as well as the number of primary FDTD cells are shown in Table I. As a reference for the

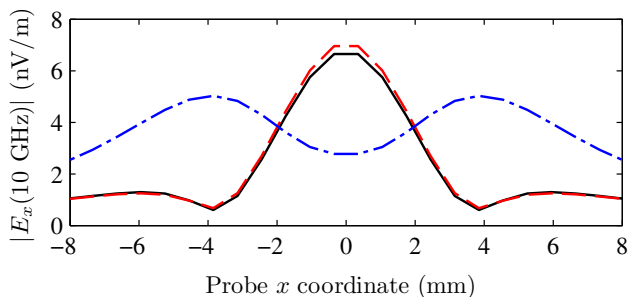


Fig. 12: Magnitude of x -directed electric field at each probe in the focusing meta-screen example of Sec. VI-C for non-uniform refinement (—), subgridding (---), and uniform coarse grid (-.-)

Table I: Computational cost for different discretization in meta-screen example of Sec. VI-C.

Method	Number of primary cells	Simulation time	Speed-up
Coarse	285,696	0.18 hours	542.0
Fine	41,997,312	99.14 hours ²	-
Nonuniform	4,936,800	13.68 hours	7.2
Proposed	1,573,416 ¹	6.81 hours	14.5

¹ Effective number of cells was larger by 8820 cells because coarse cells within the subgridding region were also updated in MATLAB implementation.

² Estimated from 30 time steps

speedup we take a simulation where uniform fine grid is used throughout the volume. Subgridding doubles the speed-up compared to the non-uniform grid refinement, which is already much faster than the full uniform grid refinement simulation. This is a result of lower number of unknowns associated with subgridding.

VII. CONCLUSION

In this work, we propose a modular and intuitive dissipation theory for analyzing stability of advanced 3-D FDTD schemes. The framework relies on showing that separate components of the system are unable to generate energy, thereby producing an overall stable scheme. As demonstrated in Sec. V-B, this approach yields simple stability proofs, which benefit from the physical intuition of the power flow. The modularity of the method allows modifying subsystems in a stable manner without burdening the stability proof. For instance, a modification to the interpolation conditions in the subgridding algorithm in Sec. V-A would only require revising dissipativity proof of the interpolation condition.

We show that a 3-D FDTD grid can be interpreted as a dissipative system if the time step satisfies the generalized CFL limit (32). Moreover, the conventional CFL limit is sufficient for dissipativity of the FDTD grid, which allows seamlessly connecting it to other dissipative subsystems.

With the new framework, we develop a stable 3-D subgridding scheme supporting material traverse. Numerical examples show good performance of the scheme when accelerating multiscale problems, as well as its ability to produce accurate and stable simulations when the subgridding interface traverses various materials. The dissipation framework is not restricted

to subgridding algorithms, and could be applied to developing more advanced schemes in the future. As a proof of concept, we have applied the dissipation framework in 2-D to FDTD involving macromodels [18].

APPENDIX

A. Proof of Equation (25)

In this section we show that equation (25) holds for any time step. Consider matrix \mathbf{L}^T defined in (17). With the following argument we show that $\mathbf{L}\mathbf{L}^T$ is a diagonal matrix that has 1's located in all diagonal entries corresponding to nonzero rows of \mathbf{B} and thus can not modify \mathbf{B} when multiplying it on the left.

Consider multiplication of a row of \mathbf{L} with a column of \mathbf{L}^T that correspond to two *different* states. The following possibilities exist

- 1) *One of the multipliers is a row or column of all zeros:* The product, which is an entry in $\mathbf{L}\mathbf{L}^T$, is clearly zero.
- 2) *Row vector $\mathbf{e}_{p_1}^T$ multiplies a column vector $\mathbf{e}_{p_2}^T$:* If the product is non-zero, then $p_1 = p_2$, i.e. the two different states are mapped to the same port on one of the faces of the region. This is not possible and hence this type of products will always yield zero entries in $\mathbf{L}\mathbf{L}^T$.
- 3) *Row vector $\mathbf{e}_{p_1}^T$ multiplies a column vector $\tilde{\mathbf{e}}_{p_2,p_3}$:* Port p_1 corresponds to an electric field of Type I and cannot be the same port as p_2 or p_3 , which map to a Type II sample. Hence, the product is zero.
- 4) *Row vector $\tilde{\mathbf{e}}_{p_1,p_2}^T$ multiplies a column vector $\mathbf{e}_{p_3}^T$:* Similarly to the previous case, the product is zero.
- 5) *Row vector $\tilde{\mathbf{e}}_{p_1,p_2}^T$ multiplies a column vector $\tilde{\mathbf{e}}_{p_3,p_4}$:* Suppose the product is non-zero. Then two different electric field samples of Type II share one or both of their corresponding ports. However, a port, or equivalently a hanging variable, can only correspond to a single electric field sample. Hence, the product must be zero.

This shows that the product $\mathbf{L}\mathbf{L}^T$ is a diagonal matrix.

Now, let us consider the diagonal entries of $\mathbf{L}\mathbf{L}^T$, which multiply rows of \mathbf{B} in the product (25). These entries result from multiplying rows of \mathbf{L} and columns of \mathbf{L}^T that correspond to the same state. The following is the exhaustive list of possible cases.

- 1) *The column of \mathbf{L}^T is zero:* This yields a zero diagonal entry in $\mathbf{L}\mathbf{L}^T$. However, the zero columns of \mathbf{L}^T correspond to states with no associated ports or hanging variables, and thus the rows of \mathbf{B} multiplied by the zero entry in $\mathbf{L}\mathbf{L}^T$ are already zero.
- 2) *The column of \mathbf{L}^T is \mathbf{e}_p :* This yields a diagonal entry of 1, which leaves the corresponding row of \mathbf{B} unchanged.
- 3) *The column of \mathbf{L}^T is $\tilde{\mathbf{e}}_{p_1,p_2}$:* This also yields a diagonal entry of 1.

This means that (25) is true. □

REFERENCES

- [1] F. Bekmambetova, X. Zhang, and P. Triverio, "A dissipative systems theory for FDTD with application to stability analysis and subgridding," *IEEE Trans. Antennas Propag.*, vol. 65, no. 2, pp. 751–762, 2017.

- [2] A. Taflove and S. C. Hagness, *Computational electrodynamics*. Artech house, 2005.
- [3] S. D. Gedney, *Introduction to the Finite-Difference Time-Domain (FDTD) Method for Electromagnetics*, 1st ed. San Rafael, CA: Morgan & Claypool Publishers, 2011.
- [4] F. Edelvik, R. Schuhmann, and T. Weiland, "A general stability analysis of FIT/FDTD applied to lossy dielectrics and lumped elements," *International Journal of Numerical Modelling: Electronic Networks, Devices and Fields*, vol. 17, no. 4, pp. 407–419, 2004.
- [5] K. Yee, "Numerical solution of initial boundary value problems involving Maxwell's equations in isotropic media," *IEEE Trans. Antennas Propag.*, vol. 14, no. 3, pp. 302–307, 1966.
- [6] M. Okoniewski, E. Okoniewska, and M. Stuchly, "Three-dimensional subgridding algorithm for FDTD," *IEEE Trans. Antennas Propag.*, vol. 45, no. 3, pp. 422–429, 1997.
- [7] P. Thoma and T. Weiland, "A consistent subgridding scheme for the finite difference time domain method," *Int. J. Numer. Model El.*, vol. 9, no. 5, pp. 359–374, 1996.
- [8] K. Xiao, D. J. Pommerenke, and J. L. Drewniak, "A three-dimensional FDTD subgridding algorithm with separated temporal and spatial interfaces and related stability analysis," *IEEE Trans. Antennas Propag.*, vol. 55, no. 7, pp. 1981–1990, 2007.
- [9] L. Kulas and M. Mrozowski, "Reduced-order models in FDTD," *IEEE Microw. Compon. Lett.*, vol. 11, no. 10, pp. 422–424, 2001.
- [10] B. Denecker, F. Olyslager, L. Knockaert, and D. De Zutter, "Generation of FDTD subcell equations by means of reduced order modeling," *IEEE Trans. Antennas Propag.*, vol. 51, no. 8, pp. 1806–1817, 2003.
- [11] T. Namiki, "A new FDTD algorithm based on alternating-direction implicit method," *IEEE Microw. Wireless Compon. Lett.*, vol. 47, no. 10, pp. 2003–2007, 1999.
- [12] F. Zheng, Z. Chen, and J. Zhang, "A Finite-Difference time-domain method without the Courant stability conditions," *IEEE Microwave Guided Wave Lett.*, vol. 9, no. 11, pp. 441–443, Nov 1999.
- [13] A. R. Bretones, R. Mittra, and R. G. Martín, "A hybrid technique combining the method of moments in the time domain and FDTD," *IEEE Microw. Guided Wave Lett.*, vol. 8, no. 8, pp. 281–283, 1998.
- [14] I. Erdin, M. S. Nakhla, and R. Achar, "Circuit analysis of electromagnetic radiation and field coupling effects for networks with embedded full-wave modules," *IEEE Trans. Electromagn. Compat.*, vol. 42, no. 4, 2000.
- [15] R. F. Remis, "On the stability of the finite-difference time-domain method," *J. Comput. Phys.*, vol. 163, pp. 249–261, 2000.
- [16] M. Mrozowski, "Stability condition for the explicit algorithms of the time domain analysis of Maxwell's equations," *IEEE Microw. Guided Wave Lett.*, vol. 4, no. 8, pp. 279–281, 1994.
- [17] L. Kulas and M. Mrozowski, "Stability of the ftd scheme containing macromodels," *IEEE Microw. Compon. Lett.*, vol. 14, pp. 484–486, 2004.
- [18] X. Zhang, F. Bekmambetova, and P. Triverio, "A Stable FDTD Method with Embedded Reduced-Order Models," *IEEE Trans. Antennas Propag.*, 2016, (submitted).
- [19] N. V. Venkatarayalu, R. Lee, Y.-B. Gan, and L.-W. Li, "A stable FDTD subgridding method based on finite element formulation with hanging variables," *IEEE Trans. Antennas Propag.*, vol. 55, no. 3, pp. 907–915, 2007.
- [20] C. Byrnes and W. Lin, "Losslessness, feedback equivalence, and the global stabilization of discrete-time nonlinear systems," *IEEE Trans. Autom. Control*, vol. 39, no. 1, pp. 83–98, 1994.
- [21] S. Boyd, L. El Ghaoui, E. Feron, and V. Balakrishnan, *Linear Matrix Inequalities in System and Control Theory*, ser. Studies in Applied Mathematics. SIAM, 1994, vol. 15.
- [22] W.-H. Steeb, *Matrix Calculus and Kronecker Product with Applications and C++ Programs*. Singapore: World Scientific, 1997.
- [23] Z. Ye, C. Liao, X. Xiong, and M. Zhang, "A novel FDTD subgridding method with improved separated temporal and spatial subgridding interfaces," *IEEE Antennas Wireless Propag. Lett.*, no. 99, 2016, (in press).
- [24] G. Kim, E. Arvas, V. Demir, and A. Z. Elsherbeni, "A novel nonuniform subgridding scheme for FDTD using an optimal interpolation technique," *Prog. Electromagn. Res. B*, vol. 44, pp. 137–161, 2012.
- [25] A. Ludwig, G. V. Eleftheriades, and C. D. Sarris, "FDTD analysis of meta-screens for sub-wavelength focusing," in *2011 IEEE International Symposium on Antennas and Propagation (APS/URSI)*, July 2011, pp. 673–676.
- [26] L. Markley, A. M. H. Wong, Y. Wang, and G. V. Eleftheriades, "Spatially shifted beam approach to subwavelength focusing," *Phys. Rev. Lett.*, vol. 101, p. 113901, 2008.